

New code for quasiequilibrium initial data of binary neutron stars: Corotating, irrotational, and slowly spinning systems

Antonios Tsokaros

*Institut für Theoretische Physik, Johann Wolfgang Goethe-Universität,
Max-von-Laue-Strasse 1, 60438 Frankfurt am Main, Germany*

Kōji Uryū

*Department of Physics, University of the Ryukyus,
Senbaru, Nishihara, Okinawa 903-0213, Japan*

Luciano Rezzolla

*Institut für Theoretische Physik, Johann Wolfgang Goethe-Universität,
Max-von-Laue-Strasse 1, 60438 Frankfurt am Main, Germany
Frankfurt Institute for Advanced Studies, Goethe University, D-60438 Frankfurt am Main, Germany
(Received 3 February 2015; published 27 May 2015)*

We present the extension of our COCAL—Compact Object CALculator—code to compute general-relativistic initial data for binary compact-star systems. In particular, we construct quasiequilibrium initial data for equal-mass binaries with spins that are either aligned or antialigned with the orbital angular momentum. The Isenberg-Wilson-Mathews formalism is adopted and the constraint equations are solved using the representation formula with a suitable choice of a Green’s function. We validate the new code with solutions for equal-mass binaries and explore its capabilities for a wide range of compactnesses, from a white dwarf binary with compactness $\sim 10^{-4}$, up to a highly relativistic neutron-star binary with compactness ~ 0.22 . We also present a comparison with corotating and irrotational quasiequilibrium sequences from the spectral code LORENE [Taniguchi and Gourgoulhon, *Phys. Rev. D* **66**, 104019 (2002)] and with different compactness, showing that the results from the two codes agree to a precision of the order of 0.05%. Finally, we present equilibria for spinning configurations with a nuclear-physics equation of state in a piecewise polytropic representation.

DOI: [10.1103/PhysRevD.91.104030](https://doi.org/10.1103/PhysRevD.91.104030)

PACS numbers: 04.25.D-, 04.25.dk, 04.30.Db, 04.40.Dg

I. INTRODUCTION

With a compactness slightly smaller than that of a black hole, neutron stars are most probably nature’s ultimate compact matter configuration before gravitational collapse and black-hole formation. As such, they present an invaluable tool to astrophysicists in order to study a plethora of problems and test the limits of existing knowledge, from general relativity, via the emission of gravitational waves, to nuclear physics, via the input on the equation of state of nuclear matter [1–5]. For example, the leading (but not unique) candidate to explain one of the most luminous explosions in the universe, the so-called short gamma-ray bursts [6,7] (see [8] for a recent review) is the merger of two neutron stars (or of one neutron star and one black hole) with the subsequent formation of a black hole, an accretion torus, and a jet structure of ultrastrong magnetic field [9,10]. Yet another example has to do with the production site of the heaviest elements in the universe through the so-called, rapid neutron capture (*r*-process) [11–16].

Central to the processes described above [17,18] is a binary neutron star system which in addition constitutes a prime source of gravitational waves for ground-based laser interferometric gravitational-wave detectors such as LIGO,

Virgo, KAGRA, and ET [19–23]. The advanced generation of these detectors will become operational in a few years, and they will be able to observe a volume of the universe a thousand times more than their predecessors. According to present estimates [24] it may be possible to detect ~ 1 –100 events per year, making the study of such systems an important step toward a practical verification of general relativity in the strong field regime, as well as an exploration of its limits. At the same time, gravitational-wave observations are expected to constrain the neutron-star equation of state [25–33].

The broad-brush picture for the two-body problem in general relativity can be divided into three phases: the inspiral, the merger, and the ring-down, with each one having its own methods and tools of investigation. The purpose of this work lies in the interface between the first and the second phases, the so-called quasiequilibrium stage, and the solutions presented are meant as “snapshots” at particular instants of the binary system. The purpose is twofold: on the one hand, to provide initial data for the simulation of the merging phase and, on the other hand, to provide evolutionary information about the system studied by constructing quasiequilibrium sequences. In this way,

we can learn how much the star shape is deformed as the orbit shrinks, where an instability sets in, where the mass-shedding limit is, and what the angular velocity of the system is there. All of this information can be computed with a modest computational infrastructure, thus allowing for the exploration of a wide parameter space.

Because the orbital decay time scale due to gravitational wave emission is much shorter than the synchronization time scale due to the neutron star viscosity, it is unlikely that the two stars will be tidally locked before merger [34,35]. For such slowly rotating configurations, the assumption of an irrotational flow is physically reasonable and mathematically simple to impose. An irrotational flow is also called a potential flow, since the fluid velocity is the gradient of a potential [36]. A formalism to compute initial data within a conformally flat geometry, the so-called Isenberg-Wilson-Mathews (IWM) formalism [37,38], was presented in Refs. [39–42], and numerical implementations for a variety of physical assumptions have been discussed by several groups [43–53]. Nonconformally flat formulations, have also been implemented [54–59], where the full system of Einstein equations is being solved. These more computationally expensive solutions are expected to respect the circularity of an orbit better than the ones coming from conformally flat initial data, which in addition seem to suppress tidal effects as the compactness of the stars increases. A conformally flat geometry can still be used to produce low eccentricity initial data if one uses ideas similar to those applied to the binary black hole problem [60], as they were implemented in [61,62].

As it was pointed in Ref. [63], the double pulsar PSR J0737-3039 has one of its stars reaching the merging epoch with a spin of ~ 27 ms, hence in a state that cannot be considered irrotational. Since we only know less than a dozen binary systems [64] and hundreds of millisecond pulsars, it is reasonable to simulate arbitrary spinning binary neutron stars and assess the impact that the stellar spin has on the gravitational-wave signal. Initial data for binary neutron stars with intermediate (and arbitrary) rotation states are more difficult to calculate, since there is no self-consistent scheme to incorporate the fluid equations with the rest of the elliptic gravitational equations. Various schemes have been proposed recently in Refs. [63,65–68], which introduce some additional approximations, while evolution of spinning binaries have been performed in [68–70].

In this work we continue the COCAL program for computing equilibrium configurations of single [71,72] and binary systems building on the infrastructure introduced in Refs. [73–75] for binary black holes. Here, we describe how to calculate initial data for binary stars, concentrating on neutron stars. The ability to compute configurations with a wide range of compactness was one of the goals of this work. At present, COCAL makes use of a piecewise polytropic description to represent the equation

of state (EOS), but fully tabulated EOSs can also be implemented. As in the vacuum case, we employ the Komatsu-Eriguchi-Hachisu (KEH) method [76–81] on multiple patches [82] in order to be able to treat binaries consisting of different compact objects. The multiple coordinates systems used in this work are not necessary for the computation of initial data coming from equal-mass binaries with spins either aligned or antialigned. In this case, in fact, it is possible to use a coordinate system positioned at the center of one compact object and employ a π symmetry to acquire the complete solution. Nevertheless, we here use three different coordinate systems (i.e., we solve all equations separately in three patches) as a first step toward solving for asymmetric binary systems, which will be presented in a future work. The gravitational equations are solved using the COCAL Poisson solvers (with appropriate Green’s functions), while for the conservation of rest mass, we follow [83] and employ the least-squared algorithm demonstrating the versatility of the methods used by our code. In this way we can calculate sequences of corotating, irrotational, as well as spinning binaries, where for the last case we use the formulation of [63] after small modifications to adapt it to our numerical methods.

The paper is organized as follows: In Sec. II we discuss the equations to be solved and the assumptions made, both for the gravitational field in Sec. II A, as well as for the fluid part in Sec. II B. For the latter we present the forms used in COCAL code for corotating, irrotational, and spinning cases. Section III represents the core of this work. In Sec. III A we briefly review the gravitational multipatch coordinate systems used in [73,74] and discuss additional changes that are related to the neutron-star surface. In Sec. III B we describe the removal of dimensions from the equations, in conjunction with the scaling introduced in Sec. III A. Section III C describes the Green’s function used for the star patch, while in Sec. III D the least-squared method for solving a spinning configuration is introduced. Tests for our new code are presented in Sec. IV A for corotating binaries and in Sec. IV B for irrotational ones, while spinning solutions with piecewise polytropes are presented in Sec. IV C. A number of appendixes provides more technical details on several topics. More specifically, Appendix A reports the expressions used for the calculation of the mass and angular momentum of the binary, Appendix B illustrates a different approach to obtain a solution of the Tolmann-Oppenheimer-Volkoff (TOV) equations, while Appendix C describes in detail the full iteration scheme and Appendix D shows tests of COCAL in a very different regime of compactness by considering binaries of white dwarfs. Finally, Appendix E reports the post-Newtonian expressions for the binding energy and orbital angular momentum of a binary system in quasicircular orbit, which are used as a reference.

Hereafter, spacetime indices will be indicated with Greek letters, and spatial indices with Latin lowercase letters. The

metric has signature $-+++$, and we use a set of geometric units in which $G = c = M_\odot = 1$, unless stated otherwise.

II. QUASIEQUILIBRIUM EQUATIONS

In this section we review the basic equations that need to be solved to obtain binary equilibrium configurations. Details of the initial-data formalism can be found in [84–87]. Here, we only mention the points that are relevant to the COCAL’s new developments.

A. The gravitational equations

One of the most fruitful ideas in simulating the circular motion of two bodies in general relativity was the introduction of helical-symmetry approximation [88,89]. Solutions with such symmetry are stationary in the corotating frame and have a long history, starting from the electromagnetic two-body problem [90]. Analogous solutions in the post-Minkowski approximation have been derived in [91,92]. Helical symmetry was also used to obtain the first law of binary star thermodynamics [93], as well as to produce equilibrium configurations of binary black holes [94,95].

Neglecting the loss of energy due to gravitational radiation and assuming closed orbits for the binary system, results in the existence of a helical Killing vector

$$k^\mu := t^\mu + \Omega\phi^\mu, \quad (1)$$

such that

$$\mathcal{L}_k g_{\alpha\beta} = 0, \quad (2)$$

where \mathcal{L}_k is the Lie derivative along k and ϕ^i is the generator of rotational symmetry. In a Cartesian coordinate system, but without loss of generality, we can assume the generator of rotational symmetry to have components

$$\phi^i = (-y, x, 0). \quad (3)$$

Writing the spacetime metric in $3+1$ form as [36,87,96,97]

$$ds^2 = -\alpha^2 dt^2 + \gamma_{ij}(dx^i + \beta^i dt)(dx^j + \beta^j dt), \quad (4)$$

where $\alpha, \beta^i, \gamma_{ij}$ are, respectively, the lapse, the shift vector, and the three-metric on Σ_t , the generator of time translations in the rotating frame can be expressed as

$$k^\mu := \alpha n^\mu + \omega^\mu. \quad (5)$$

Here, $\omega^\mu := \beta^\mu + \Omega\phi^\mu$ is the corotating shift, and n^μ the unit normal to Σ_t , $n_\mu := -\alpha\nabla_\mu t$. Since $\mathcal{L}_k\gamma_{ij} = 0 = \mathcal{L}_k K_{ij}$, the evolution equation of γ_{ij} specifies the extrinsic curvature in terms of the shift and the lapse

$$K_{ij} = \frac{1}{2\alpha}(D_i\omega_j + D_j\omega_i), \quad (6)$$

where D is the derivative operator associated with γ_{ij} . The traceless extrinsic curvature

$$A_{ij} := K_{ij} - \frac{1}{3}K^m{}_m\gamma_{ij} = K_{ij} - \frac{1}{3}K\gamma_{ij} \quad (7)$$

can be written in terms of the longitudinal operator \mathbb{L} ,

$$\begin{aligned} A_{ij} &= \frac{1}{2\alpha}\left(D_i\omega_j + D_j\omega_i - \frac{2}{3}\gamma_{ij}D_k\omega^k\right) \\ &:= \frac{1}{2\alpha}(\mathbb{L}\omega)_{ij}. \end{aligned} \quad (8)$$

Assuming a maximal and conformally flat slice [37,38]

$$\gamma_{ij} = \psi^4\delta_{ij}, \quad (9)$$

the traceless extrinsic curvature Eq. (8) is written in terms of the shift

$$\begin{aligned} A^{ij} &= \frac{\psi^{-4}}{2\alpha}\left(\partial^i\beta^j + \partial^j\beta^i - \frac{2}{3}\delta^{ij}\partial_k\beta^k\right) \\ &= \frac{\psi^{-4}}{2\alpha}(\tilde{\mathbb{L}}\beta)^{ij}. \end{aligned} \quad (10)$$

The tilde symbol on the longitudinal operator \mathbb{L} denotes the fact that it is related to the conformally flat geometry. In deriving Eq. (10) use has been made of the fact that $\partial_i\phi^i = 0 = \partial_{(i}\phi_{j)}$ [cf. Eq. (3)]. In the conformally flat geometry, the contravariant components of the shift remain the same as in the original spatial geometry (i.e., $\tilde{\beta}^i = \beta^i$), while this is not true for the covariant components.

With the help of Eq. (10), the constraint equations and the spatial trace of the time derivative of the extrinsic curvature result in five elliptic equations for the conformal factor ψ , the shift β^i , and the lapse function α ,

$$\begin{aligned} \nabla^2\psi &= -\frac{\psi^5}{32\alpha^2}(\tilde{\mathbb{L}}\beta)^{ab}(\tilde{\mathbb{L}}\beta)^{ij}\delta_{ia}\delta_{jb} - 2\pi E\psi^5 \\ &:= S_\psi^g + S_\psi^f, \end{aligned} \quad (11)$$

$$\begin{aligned} \nabla^2(\alpha\psi) &= \frac{7\psi^5}{32\alpha}(\tilde{\mathbb{L}}\beta)^{ab}(\tilde{\mathbb{L}}\beta)^{ij}\delta_{ia}\delta_{jb} + 2\pi\alpha\psi^5(E + 2S) \\ &:= S_\alpha^g + S_\alpha^f, \end{aligned} \quad (12)$$

$$\begin{aligned} \nabla^2\beta^i &= -\frac{1}{3}\partial^i\partial_j\beta^j + \partial_j\ln\left(\frac{\alpha}{\psi^6}\right)(\tilde{\mathbb{L}}\beta)^{ij} + 16\pi\alpha\psi^4 j^i \\ &:= S_\beta^g + S_\beta^f. \end{aligned} \quad (13)$$

We have denoted with S_α^f the sources of the Poisson-type equations that come from the energy-momentum tensor, while with S_α^g are the sources that come from the nonlinear part of the Einstein tensor $G_{\alpha\beta}$. The matter sources in Eqs. (11)–(13), $S_\psi^f, S_\alpha^f, S_\beta^f$, are related to the corresponding projections of the energy-momentum tensor

$$E := n_\alpha n_\beta T^{\alpha\beta}, \quad (14)$$

$$S := \gamma_{\alpha\beta} T^{\alpha\beta}, \quad (15)$$

$$j^i := -\gamma_\alpha^i n_\beta T^{\alpha\beta}, \quad (16)$$

where E is the energy density as measured by a “normal” observer, that is, an observer with four-velocity \mathbf{n} . Note also that since we use $G = c = M_\odot = 1$, all quantities in equations (11)–(13) are dimensionless. This is contrary to some previous works (e.g., [46]), where only $G = c = 1$ was assumed, and a procedure to remove units was applied through the use of the adiabatic constant K . Here the normalization scheme used is explained in detail in Sec. III B.

The above set of equations must be supplied with conditions on the boundary of our computational region. Since we will consider only binary stars, our boundary for the gravitational equations will be only at spatial infinity, where we impose asymptotic flatness, i.e.,

$$\lim_{r \rightarrow \infty} \psi = 1, \quad \lim_{r \rightarrow \infty} \alpha = 1, \quad \lim_{r \rightarrow \infty} \beta^i = 0. \quad (17)$$

We recall that a helically symmetric spacetime cannot be asymptotically flat, because a helically symmetric binary produces an infinite amount of radiation. Therefore conditions (17) seem to contradict assumption (1). In reality, the helical symmetry is only an approximation that is valid either for long times when the binary is widely separated or for only a short time when the binary is tight. In practice, the emission of gravitational radiation reaction will lead to an inspiral, thus breaking the symmetry.

B. The fluid equations

Let u^α be the four-velocity of the fluid. We consider a perfect fluid with energy-momentum tensor [36,98]

$$T_{\alpha\beta} = (\epsilon + p)u_\alpha u_\beta + pg_{\alpha\beta} = \rho h u_\alpha u_\beta + pg_{\alpha\beta}, \quad (18)$$

where ρ, ϵ, h , and p are, respectively, the rest-mass density, the total energy density, the specific enthalpy, and the pressure as measured in the rest frame of the fluid. The specific internal energy e is related to the enthalpy through¹

¹Note that many authors use e and ϵ to indicate the energy density and the specific internal energy, respectively.

$$h := \frac{\epsilon + p}{\rho} = 1 + e + \frac{p}{\rho}. \quad (19)$$

The first law of thermodynamics, $de = \rho T ds + h d\rho$, where s is the specific entropy, written in terms of the specific enthalpy h , reads $dh = T ds + dp/\rho$. For isentropic configurations, like the quasiequilibrium solutions we are seeking, given an EOS which relates, for example, the pressure p with the rest-mass energy density ρ , we can see that the extra variables that enter our problem are ρ (or p) and the four-velocity u^α . For these new variables, extra equations need to be used exploiting conservation laws. In particular, from the conservation of the energy-momentum tensor

$$0 = \nabla_\alpha T^{\alpha\beta} = \rho [u^\alpha \nabla_\alpha (h u^\beta) + \nabla^\beta h] + h u^\beta \nabla_\alpha (\rho u^\alpha) - \rho T \nabla^\beta s, \quad (20)$$

assuming isentropic configurations and local conservation of rest mass²

$$\nabla_\alpha (\rho u^\alpha) = 0, \quad (21)$$

we arrive at the relativistic Euler equation

$$u^\alpha \nabla_\alpha (h u_\beta) + \nabla_\beta h = 0. \quad (22)$$

Although we use four-dimensional indices, this is a fully spatial equation, since the projection along the fluid flow is trivially satisfied. Equations (21) and (22) provide us with four more equations for the fluid variables. If one of them is used for the determination of ρ , we are left with three equations that must determine the four-velocity u^α , which has only three independent components.

Expressing the four-velocity as $u^\alpha = u^t(1, v^i)$ and in analogy with a Newtonian decomposition, we can split the spatial component v^i into two parts: one that follows the orbital path ϕ^i , and one that represents the velocity in the corotating frame V^i . Using the helical Killing vector, Eq. (1), we can write

$$u^\alpha = u^t(k^\alpha + V^\alpha), \quad (23)$$

where the spatial part, $V^\alpha = (0, V^i)$, can be considered to be the “nonrotating” part of the fluid flow (i.e., the velocity in the corotating frame). The conservation of rest mass (21) and the spatial projection of the Euler equation (22), written in 3 + 1 form, translate to

²More precisely, the Euler equation is the projection orthogonal to the fluid flow of the conservation of the energy-momentum tensor and leads to three distinct spatial equations. On the other hand, the projection along the flow of $\nabla_\alpha T^{\alpha\beta} = 0$ yields a single equation expressing energy conservation [36].

$$\mathcal{L}_k(\rho u^t) + \frac{1}{\alpha} D_i(\alpha \rho u^t V^i) = 0, \quad (24)$$

$$\begin{aligned} \gamma_i^\alpha \mathcal{L}_k(hu_\alpha) + D_i \left(\frac{h}{u^t} + hu_j V^j \right) \\ + V^j (D_j(hu_i) - D_i(hu_j)) = 0. \end{aligned} \quad (25)$$

The last term of Eq. (25) involves the relativistic vorticity tensor [36]

$$\omega_{\alpha\beta} := \nabla_\alpha(hu_\beta) - \nabla_\beta(hu_\alpha) \quad (26)$$

and is zero for an irrotational flow. It is not difficult to show that in the presence of a generic Killing vector field (e.g., the helical Killing field) \mathbf{k} , the following identity holds [36]:

$$\mathcal{L}_u(h\mathbf{u} \cdot \mathbf{k}) = 0. \quad (27)$$

In the case of a rigid corotation of the binary system, $\mathbf{u} = \mathbf{k}$, so that the Lie derivative along the fluid four-velocity \mathbf{u} in Eq. (27) can be replaced by the Lie derivative along the helical Killing vector \mathbf{k} . This yields $\mathcal{L}_k h = 0$ and expresses that in the corotating frame the fluid properties do not change. When the fluid four-velocity does not coincide with the helical Killing field, but the two vector fields are not too different; i.e., when $\mathbf{u} \approx \mathbf{k}$, expression (27) can still be true and indeed for the flows we will consider hereafter we will assume the following assumption:

$$\gamma_i^\alpha \mathcal{L}_k(hu_\alpha) = 0 = \mathcal{L}_k(\rho u^t). \quad (28)$$

While Eq. (28) is an assumption, its correctness can only be assessed *a posteriori* and could indeed not represent a valid approximation if the stars are spinning very rapidly, a case we will not investigate here.

In the following we will specialize Eqs. (24) and (25) under the assumption (28) for corotating, irrotational, and slowly rotating flows. Before closing we introduce a quantity that will be used often in subsequent sections, namely, the spatial projection of the specific enthalpy current

$$\hat{u}_i := \gamma_i^\alpha hu_\alpha. \quad (29)$$

1. Corotating binaries

The corotating case, also called of rigid rotation [99,100], is the simplest case, since the spatial fluid velocity V^i vanishes, $u^\alpha = u^t k^\alpha$, and thus the fluid is at rest in a corotating frame. This means that apart from the gravitational variables ψ, α, β^i , we have only two extra fluid variables, for example, ρ and u^t once an EOS is fixed. The conservation of rest mass (24) is trivially satisfied, while

the Euler equation (25) becomes a single integral equation that, together with the normalization condition $u^\alpha u_\alpha = -1$, will determine all our fluid variables.

In particular, the specific enthalpy current becomes

$$\hat{u}^i = hu^t \omega^i, \quad (30)$$

and from the four-velocity normalization condition we have

$$u^t = \frac{1}{\sqrt{\alpha^2 - \omega_i \omega^i}}. \quad (31)$$

Equation (25), on the other hand, has the first integral

$$\frac{h}{u^t} = C, \quad (32)$$

where C is a constant to be determined. Equations (31) and (32), together with the gravitational potentials, completely determine the solution for this case. We note that in all equations to be solved (the gravitational ones included) two constants are involved. One is C , the constant that comes from the Euler integral, and one is Ω , the orbital angular velocity. Thus, in order to be able to achieve a solution for our system, a self-consistent scheme that involves the determination of both C and Ω must be employed. As we will elaborate later on, this will be achieved in conjunction with the determination of the length scale R_0 of our problem.

For the corotating case the matter sources in Eqs. (11)–(13) are

$$E = \rho[h(\alpha u^t)^2 - q], \quad (33)$$

$$E + 2S = \rho[h[3(\alpha u^t)^2 - 2] + 5q], \quad (34)$$

$$j^i = \rho \alpha u^t \hat{u}^i, \quad (35)$$

where $q := p/\rho$. As we have already mentioned, all quantities appearing above are dimensionless, while in previous studies, where geometric units were used, Eqs. (33)–(35) had units of length⁻².

2. Irrotational and spinning binaries

Irrotational configurations have $\omega_{\alpha\beta} = 0$, so that the specific enthalpy current hu_α can be derived from a potential [36], i.e.,

$$hu_\alpha = \nabla_\alpha \Phi = D_\alpha \Phi + n_\alpha \mathcal{L}_n \Phi, \quad (36)$$

so that $\hat{u}_i = D_i \Phi$ since $\boldsymbol{\gamma} \cdot \mathbf{n} = 0$. To allow for spinning configurations we need to extend expression (36), and we do this following Ref. [67] and introducing a four-vector s (not to be confused with the specific entropy s)

$$hu_\alpha = \nabla_\alpha \Phi + s_\alpha, \quad (37)$$

so that \hat{u}^i is decomposed as

$$\hat{u}^i = D^i \Phi + s^i, \quad (38)$$

where the $D^i \Phi$ part corresponds to the “irrotational part” of the flow and the s^i part to the “spinning part” of the flow. In what follows we will present expressions for spinning binaries ($s^i \neq 0$), and one can recover the irrotational ones by setting the spinning component s^i equal to zero.

Using the decomposition (38) and the assumption (28), the Euler equation (25) can be rewritten as

$$\mathcal{L}_V s_i + D_i \left(\frac{h}{u^t} + V^j D_j \Phi \right) = 0, \quad (39)$$

and hereafter we will assume

$$\mathcal{L}_V s_i = 0, \quad (40)$$

which is likely to be a very good approximation in the case of slowly and uniformly rotating stars, for which s_i is intrinsically small.³ Hence, the Euler equation for generic binaries (25)

$$\gamma_i^\alpha [\mathcal{L}_k(hu_\alpha) + \mathcal{L}_V(s_\alpha)] + D_i \left(\frac{h}{u^t} + V^j D_j \Phi \right) = 0, \quad (41)$$

under the assumptions (28) and (40), yields the reduced Euler integral

$$\frac{h}{u^t} + V^j D_j \Phi = C, \quad (42)$$

where again C is a constant to be determined. A few remarks should be made at this point. First, it is not difficult to obtain the following identity:

$$\begin{aligned} \gamma_i^\alpha [\mathcal{L}_k(hu_\alpha) + \mathcal{L}_V(s_\alpha)] \\ = \gamma_i^\alpha [\mathcal{L}_k(\nabla_\alpha \Phi) + \mathcal{L}_{\nabla \Phi / (hu^t)}(s_\alpha) + \mathcal{L}_{s / (hu^t)}(s_\alpha)], \end{aligned} \quad (43)$$

so that our assumptions (28) and (40),

$$\gamma_i^\alpha \mathcal{L}_k(hu_\alpha) = 0 = \gamma_i^\alpha \mathcal{L}_V(s_\alpha), \quad (44)$$

are equivalent to setting the left-hand side of Eq. (43) to zero. In turn, this implies that also the right-hand side of (43) is zero, which is true if, for instance, each of the three terms is zero, i.e., if

³In practice we will consider stars with spin period down to 0.6 ms, but this is still “slowly” spinning when compared to the minimum period.

$$\gamma_i^\alpha \mathcal{L}_k(\nabla_\alpha \Phi) = 0 = \gamma_i^\alpha \mathcal{L}_{\nabla \Phi / (hu^t)}(s_\alpha) = \gamma_i^\alpha \mathcal{L}_{s / (hu^t)}(s_\alpha). \quad (45)$$

The three conditions in (45) coincide with the assumptions made in [63]. Stated differently, because the conditions (44) are compatible with the conditions (45), it does not come as a surprise that we obtain the same Euler integral (42) as in [63] despite making apparently different assumptions [cf. (44) versus (45)]. Second, using the decomposition (37), it follows that

$$\gamma_i^\alpha \mathcal{L}_k(hu_\alpha) = \gamma_i^\alpha [\mathcal{L}_k(\nabla_\alpha \Phi) + \mathcal{L}_k(s_\alpha)], \quad (46)$$

and hence the question about $\mathcal{L}_k(hu_\alpha) = 0$ depends on both $\mathcal{L}_k(\nabla_\alpha \Phi)$ and $\mathcal{L}_k(s_\alpha)$ being zero.⁴ The second term is essentially an input to our problem, while the first one comes from the conservation of rest mass (57), which depends on the spin input s_α . Finally, although the Euler integral has the same form for both irrotational and spinning binaries, it produces a different equation since the three-velocity V^i is different in these two cases. More specifically, it is

$$\hat{u}^i = hu^t(\omega^i + V^i), \quad (47)$$

so that

$$V^i = \frac{D^i \Phi + s^i}{hu^t} - \omega^i. \quad (48)$$

In this case, the fluid variables are ρ (or equivalently p or h), u^t , and the fluid potential Φ . The equations that will determine them are the normalization condition $u_\alpha u^\alpha = -1$, the Euler integral (42) [with the use of Eq. (48)], and the conservation of rest mass (24).

In particular, from the norm of \hat{u}^i we get

$$h = \sqrt{\alpha^2 (hu^t)^2 - (D_i \Phi + s_i)(D^i \Phi + s^i)}, \quad (49)$$

therefore, the Euler integral (42) takes the following form quadratic in hu^t :

$$\alpha^2 (hu^t)^2 - \lambda (hu^t) - s_i (D^i \Phi + s^i) = 0, \quad (50)$$

where $\lambda = C + \omega^i D_i \Phi$. Thus

$$hu^t = \frac{\lambda + \sqrt{\lambda^2 + 4\alpha^2 s_i (D^i \Phi + s^i)}}{2\alpha^2}, \quad (51)$$

where we take the positive root since the negative one is incorrect at least in the limit of $s^i = 0$, when it yields $hu^t = 0$.

⁴Note that even when the spins are aligned with the orbital angular momentum $\mathcal{L}_k(s_\alpha) \neq 0$.

Having computed λ , we first calculate hu^t from Eq. (51), and then h from Eq. (49). For purely irrotational binaries $hu^t = \lambda/\alpha^2$ and $h = \sqrt{\lambda^2/\alpha^2 - D_i\Phi D^i\Phi}$.

Although we will not make immediate use of u^t and h separately, we report below their form for completeness

$$h = \sqrt{L^2 - (D_i\Phi + s_i)(D^i\Phi + s^i)}, \quad (52)$$

$$u^t = \frac{\sqrt{h^2 + (D_i\Phi + s_i)(D^i\Phi + s^i)}}{h\alpha}, \quad (53)$$

where

$$L^2 := \frac{\lambda^2 + 2\alpha^2 W + \lambda\sqrt{\lambda^2 + 4\alpha^2 W}}{2\alpha^2}, \quad (54)$$

$$W := s_i(D^i\Phi + s^i). \quad (55)$$

The potential Φ will be computed from the conservation of rest mass (24), which under Eq. (48), and after expressing the spin velocity as a power law [63]

$$s^i = \psi^A \tilde{s}^i, \quad A \in \mathbb{R}, \quad (56)$$

will produce an extra elliptic equation

$$\begin{aligned} \nabla^2 \Phi = & -\frac{2}{\psi} \partial_i \psi \partial^i \Phi + \psi^4 \omega^i \partial_i (hu^t) \\ & + [\psi^4 hu^t \omega^i - \partial^i \Phi] \partial_i \ln\left(\frac{\alpha\rho}{h}\right) \\ & - \psi^{4+A} \left[\partial_i \tilde{s}^i + \tilde{s}^i \partial_i \ln\left(\frac{\alpha\rho\psi^{6+A}}{h}\right) \right] = S_\Phi. \end{aligned} \quad (57)$$

The boundary for the fluid is represented by the surface of the star; hence the boundary condition for Eq. (57) will be of von Neumann type, that is, in terms of derivatives of the rest-mass density and of Φ

$$[(\psi^4 hu^t \omega^i - \partial^i \Phi - \psi^{4+A} \tilde{s}^i) \partial_{i\rho}]_{\text{surf}} = 0. \quad (58)$$

A possible and convenient choice for the parameter A that will be used in Sec. IV C is $A = -6$, as it removes the last term in Eq. (57).⁵ Any other value will not change the character of the equation or the boundary condition, although it will change the detailed properties of the flow velocity and therefore of the binary. We will comment on this point in Sec. IV C, where we will also illustrate the results for $A = 0$.

For the spinning case, the matter sources in Eqs. (11)–(13) are

⁵More precisely, $A = -6$ makes the spin have zero divergence in the three-geometry ($D_i s^i = 0$) if we choose it to have zero divergence in the conformal three-geometry ($\tilde{D}_i \tilde{s}^i = 0$).

$$E = \rho \left[\frac{\alpha^2}{h} (hu^t)^2 - q \right], \quad (59)$$

$$E + 2S = \rho \left[3 \frac{\alpha^2}{h} (hu^t)^2 - 2h + 5q \right], \quad (60)$$

$$j^i = \rho \alpha u^t \hat{u}^i = \rho \frac{\alpha}{h} (hu^t) [\psi^{-4} \partial^i \Phi + \psi^A \tilde{s}^i], \quad (61)$$

where we have used Eq. (51) to simplify the calculations.

C. Equation of state

The EOS used in this work is represented by a sequence of polytropes called a piecewise polytrope. This is proven to be a good approximation for a great variety of models [101–104]. If N is the number of such polytropes, in each piece the pressure and the rest-mass density are

$$p = K_i \rho^{\Gamma_i}, \quad i = 1, 2, \dots, N. \quad (62)$$

The order of the polytropes is $i = 1$ for the crust and $i = N$ for the core, and Eq. (62) holds for

$$\rho_{i-1} \leq \rho < \rho_i. \quad (63)$$

As we have discussed in Sec. II B, the first law of thermodynamics for isentropic configurations gives $dh = dp/\rho$, which can be expressed in terms of q to yield

$$dh = \frac{\Gamma_i}{\Gamma_i - 1} dq, \quad (64)$$

or equivalently

$$h - h_i = \frac{\Gamma_i}{\Gamma_i - 1} (q - q_i), \quad (65)$$

where h_i, q_i correspond to values at the right end point (the one closest to the core) of the i th interval. In terms of q , we can express the rest of thermodynamic variables as

$$\rho = K_i^{1/(1-\Gamma_i)} q^{1/(\Gamma_i-1)}, \quad (66)$$

$$p = K_i^{1/(1-\Gamma_i)} q^{\Gamma_i/(\Gamma_i-1)}, \quad (67)$$

$$\epsilon = \rho h - p. \quad (68)$$

Enforcing the continuity of the pressure at the $N - 1$ interfaces of each interval constraints all adiabatic constants K_i but one

$$K_i \rho_i^{\Gamma_i} = K_{i+1} \rho_i^{\Gamma_{i+1}}. \quad (69)$$

As a result, the free parameters are one adiabatic constant, $N - 1$ rest-mass densities, and N adiabatic indices, a total of $2N$ parameters.

III. NUMERICAL METHOD

The COCAL code for binary black holes has been described in detail in Refs. [73–75]. Here, we will review the most salient features of the grids used for the solution of the field equations and discuss the differences that arise from the treatment of binary stars.

When treating binary systems, COCAL employs two kinds of coordinate systems. The first kind is compact object coordinate patch (COCP) and has exactly two members, one centered on each star. The second kind is asymptotic region coordinate patch (ARCP) and can have in principle any number of members in an onion type of structure. In our computations, the ARCP patch has only one member, which is centered on the center of mass of the system. All coordinate systems use spherical coordinates $(r, \theta, \phi) \in [r_a, r_b] \times [0, \pi] \times [0, 2\pi]$, but the components of field variables (like the shift) are written with their Cartesian components $(\beta^x, \beta^y, \beta^z)$. The values of r_a, r_b depend on the compact object (black hole or neutron star) and the coordinate patch (COCP or ARCP). For the binary systems treated here, r_a of the COCP patch will always be zero, while for the ARCP patch $r_a \approx \mathcal{O}(10M)$, M being the mass of the star. As for r_b , the values are kept the same as in the binary black hole computation, i.e., $\mathcal{O}(10^2M)$ for the COCP patch, and $\mathcal{O}(10^6M)$ for the ARCP patch.

The orientation of the coordinate patches is as follows: the ARCP patch has the familiar (x, y, z) orientation, the first COCP patch, which is centered on the negative x axis of the ARCP patch, has the same orientation as the ARCP patch, while the second COCP patch, which is centered on the positive x axis of the ARCP patch, has negative (x, y) orientation, and positive z orientation with respect to the ARCP patch and to the first COCP patch. In other words, the coordinate system of the second COCP patch is obtained from the first COCP patch by a rotation through an angle of π .

The geometry of the ARCP patch (or any number of them) is that of a solid spherical shell with inner radius r_a and outer radius r_b . On the other hand, the COCP patch geometry is that of a sphere of radius r_b , with another sphere of radius r_e at distance d_s from the center, being removed from its interior. This second sphere whose boundary we call the excised sphere S_e , is centered on the x axis around the *other* compact object. For the first COCP patch, its excised sphere S_e is centered on the position of the second star, while for the second COCP patch, its excised sphere S_e is centered on the position of the first star. The size of every sphere S_e is slightly larger than the star resolved with an opening half-angle of $\sim \pi/3$ as seen from the origin of the COCP patch. This is done to resolve accurately the region around the *other* star and

TABLE I. Summary of grid the parameters used for the binary systems computed here.

r_a :	Radial coordinate where the radial grids start. For the COCP patch it is $r_a = 0$.
r_b :	Radial coordinate where the radial grids end.
r_c :	Center of mass point. Excised sphere is located at $2r_c$ in the COCP patch.
r_e :	Radius of the excised sphere. Only in the COCP patch.
r_s :	Radius of the sphere bounding the star's surface. It is $r_s \leq 1$. Only in COCP.
N_r :	Number of intervals Δr_i in $r \in [r_a, r_b]$.
N_r^1 :	Number of intervals Δr_i in $r \in [0, 1]$. Only in the COCP patch.
N_r^f :	Number of intervals Δr_i in $r \in [0, r_s]$ in the COCP patch or $r \in [r_a, r_a + 1]$ in the ARCP patch.
N_r^m :	Number of intervals Δr_i in $r \in [r_a, r_c]$.
N_θ :	Number of intervals $\Delta \theta_j$ in $\theta \in [0, \pi]$.
N_ϕ :	Number of intervals $\Delta \phi_k$ in $\phi \in [0, 2\pi]$.
d :	Coordinate distance between the center of S_a ($r = 0$) and the center of mass.
d_s :	Coordinate distance between the center of S_a ($r = 0$) and the center of S_e .
L :	Order of included multipoles.

reduce the number of multipoles used in the Legendre expansion. In this work we typically use 12 multipoles in our computations. Table I summarizes the properties of the various coordinate patches used and which are illustrated schematically in Fig. 1.

On the coordinate grids described above we solve the Poisson-type nonlinear equations (11), (12), and (13). These equations are solved using the representation formula with a suitable choice of a Green's function (this is also known as the KEH method [81]). The Green's function is expanded in terms of spherical harmonics, and the integrals (both volume and surface) are performed on the spherical coordinate grids described above and in more detail in Sec. III A for the case of binary stars.

The numerical approximations introduced in COCAL are of different types: First, from the truncation of the series of the Legendre expansion; second, from the solution of the equations on discretized grids via finite-difference methods [36]. Typically, we use second-order centered stencils for the numerical differentiations and integrations [73]. An exception is the use of a third-order finite-difference stencil for the radial derivatives and the use of a fourth-order integration in the polar coordinate [74]. We also typically use second-order interpolations of scalar functions from grid points to midpoints. Furthermore, when a function needs to be interpolated from one coordinate system to another, we use a fourth-order Lagrange interpolation. This usually happens when we compute the surface integral at the excised sphere S_e for in that case we need the potential and its derivative on S_e as seen from the center of S_e .

$$\Delta r_i = \Delta r, \quad \text{for } i = 1, \dots, N_r^f - 1, \quad (70)$$

$$\Delta r_{i+1} = h_1 \Delta r_i, \quad \text{for } i = N_r^f, \dots, N_r^1 - 1, \quad (71)$$

$$\Delta r_i = \Delta r_2, \quad \text{for } i = N_r^1, \dots, N_r^m, \quad (72)$$

$$\Delta r_{i+1} = h_3 \Delta r_i, \quad \text{for } i = N_r^m, \dots, N_r^m + N_r^1 - 1, \quad (73)$$

$$\Delta r_{i+1} = h_4 \Delta r_i, \quad \text{for } i = N_r^m + N_r^1, \dots, N_r - 1, \quad (74)$$

which correspond to regions *S*, *I*, *II*, *III*, and *IV*, respectively. The ratios $h_i (> 1)$ ($i = 1, 3, 4$) are, respectively, determined from the relations

$$1 - r_s = \Delta r \frac{h_1(h_1^{N_r^1 - N_r^f} - 1)}{h_1 - 1}, \quad (75)$$

$$2r_c = \Delta r \frac{h_3(h_3^{N_r^f} - 1)}{h_3 - 1}, \quad (76)$$

$$r_b - 3r_c = \Delta r \frac{h_4(h_4^{N_r - N_r^m - N_r^f} - 1)}{h_4 - 1}. \quad (77)$$

For the ARCP coordinate system, there are in general two regions, one with constant grid spacing and one with increasing spacing. The grid intervals in these regions are defined by

$$\Delta r_i = \Delta r_1, \quad \text{for } i = 1, \dots, N_r^m, \quad (78)$$

$$\Delta r_{i+1} = k \Delta r_i, \quad \text{for } i = N_r^m, \dots, N_r - 1, \quad (79)$$

where $\Delta r_1 = 1/N_r^f$, and the ratio k is determined from

$$r_b - r_c =: \Delta r \frac{k(k^{N_r - N_r^m} - 1)}{k - 1}. \quad (80)$$

As regards the angular resolution, we keep the same grid interval in the θ and ϕ directions and therefore

$$\Delta \theta_j = \theta_j - \theta_{j-1} = \Delta \theta = \frac{\pi}{N_\theta}, \quad (81)$$

$$\Delta \phi_k = \phi_k - \phi_{k-1} = \Delta \phi = \frac{2\pi}{N_\phi}. \quad (82)$$

One of the additional complications of having to deal with the fluid of a star, instead of a vacuum spacetime, is the need to accurately find its surface. This surface may contract or expand during the calculation, creating significant problems in close binary configurations. One very effective solution to these issues [105] is the use of *surface-fitted coordinates* (SFC) that exist only inside each fluid and are normalized by the radius of the star. We denote this extra spherical coordinate system as (r_f, θ_f, ϕ_f) , where

$$r_f := \frac{r}{R(\theta, \phi)}, \quad \theta_f := \theta, \quad \phi_f := \phi, \quad (83)$$

and where the surface of the star is denoted by $R(\theta, \phi)$.

By construction, the domain of these fluid coordinates is $[0, 1] \times [0, \pi] \times [0, 2\pi]$, and $R(\theta_f, \phi_f)$ is a function that will be determined at the end of the self-consistent iterative method (see Appendix C). The advantage of SFC in the computation of derivatives on the star's surface, as well as the implementation of the boundary condition Eq. (58), will be discussed in Sec. III D.

B. Dimensionless and normalized variables

Having removed the dimensions from our equations by using units in which $G = c = M_\odot = 1$, we perform a normalization of all variables in order to introduce a scale in our problem that is intimately related to the variable r_s , introduced in Sec. III A.

We normalize variables by demanding that the intersection of the star's surface with the positive x axis be at $r = r_s$. If R_0 is the scaling parameter, we impose⁶

$$\frac{R(\pi/2, 0)}{R_0} = r_s = \frac{R(\pi/2, \pi)}{R_0}, \quad (84)$$

so that $r_s R_0$ is the real semimajor radius of the star. Hereafter, we will denote normalized variables with a hat and thus define

$$\hat{x}^i := \frac{x^i}{R_0}, \quad (85)$$

from which it follows that the normalized version of Eq. (11) is⁷

$$\hat{\nabla}^2 \psi = \hat{S}_\psi^g + R_0^2 S_\psi^f, \quad (86)$$

where $\hat{\nabla}$ is the Laplacian operator associated with the variables \hat{x}^i , and similarly \hat{S}_ψ^g has all derivatives with respect to the normalized variables. Note also that

$$\omega^i = \beta^i + \Omega \phi^i = \beta^i + \hat{\Omega} \hat{\phi}^i, \quad (87)$$

where $\hat{\Omega} := \Omega R_0$. If we now define

$$\hat{\Phi} := \frac{\Phi}{R_0}, \quad (88)$$

we observe that all scaling factors in Eq. (57) drop out. Because this is also true for the boundary condition, i.e.,

⁶Note that r_s , but also r_f in Eq. (83), are ratios of two radial coordinates and thus dimensionless for any choice of units; in this respect, they do not need to be indicated with a hat.

⁷Similar normalized equations hold for Eqs. (12) and (13).

Eq. (58), these equations are each coded in the same form but with normalized quantities replacing the original ones.

Before proceeding further with our normalization scheme, let us comment that the surface-fitted coordinates of Eq. (83) are already normalized coordinates and their radial range is $[0, 1]$ irrespective of the fluid scaling profile r_s . Since $R(\theta, \phi) \leq R(\pi/2, 0) = R_0 r_s$, we have $0 \leq r \leq R(\theta, \phi) \leq R_0 r_s$, so that the range for \hat{r} is

$$\hat{r} \leq \hat{R}(\theta, \phi) \leq r_s, \quad \text{or} \quad r_f = \frac{\hat{r}}{\hat{R}(\theta, \phi)} \leq 1. \quad (89)$$

Changing the scale by modifying R_0 will affect the conformal factor and the lapse function since they scale as [46,106]

$$\psi = \hat{\psi}^{R_0^2}, \quad \alpha = \hat{\alpha}^{R_0^2}. \quad (90)$$

As mentioned earlier, the system of partial differential equations that we have to solve, i.e., the normalized versions of Eqs. (11)–(13) and Eq. (57), involve three constants: R_0 , $\hat{\Omega}$, and C . To find them we will use the Euler integral evaluated at three arbitrary points to construct a nonlinear 3×3 system that will be solved with a typical Newton-Raphson method. This procedure will be repeated every time we solve for any of the unknown variables ψ , β^i , α , Φ , and q , since any change of them will affect the Euler integral and thus the three constants.

The arbitrary points we choose to evaluate the Euler integral are along the x axis and in spherical coordinates are defined as

$$r_1 = r_s, \quad \theta_1 = \pi/2, \quad \phi_1 = 0, \quad (91)$$

$$r_2 = 0, \quad \theta_2 = 0, \quad \phi_2 = 0, \quad (92)$$

$$r_3 = r_s, \quad \theta_3 = \pi/2, \quad \phi_3 = \pi. \quad (93)$$

In the corotating case, Eqs. (32) and (31) will become

$$F_c(\hat{\Omega}, R_0, C) = -\ln C + R_0^2 \ln \hat{\alpha} + \ln h + \frac{1}{2} \ln \left[1 - \left(\frac{\hat{\psi}^2}{\hat{\alpha}} \right)^{2R_0^2} (\beta^y + \hat{\Omega} \hat{\phi}^y)^2 \right] = 0, \quad (94)$$

while for the spinning case, Eqs. (42), (49), and (51) yield

$$F_{is}(\hat{\Omega}, R_0, C) = -\ln \lambda + R_0^2 \ln \hat{\alpha} + \ln h - \ln \left[\frac{1}{2} + \sqrt{\frac{1}{4} + \frac{A(R_0)}{\lambda^2}} \right] + \frac{1}{2} \ln \left[1 + \frac{B(R_0)}{h^2} \right] = 0, \quad (95)$$

with

$$A(R_0) := (\hat{\alpha}^2 \hat{\psi}^A)^{R_0^2} \tilde{s}^i \hat{\partial}_i \hat{\Phi} + (\hat{\alpha}^2 \hat{\psi}^{4+2A})^{R_0^2} \delta_{ij} \tilde{s}^i \tilde{s}^j, \\ B(R_0) := (\hat{\psi}^{-4})^{R_0^2} \hat{\partial}_i \hat{\Phi} \hat{\partial}^i \hat{\Phi} + 2(\hat{\psi}^A)^{R_0^2} \tilde{s}^i \hat{\partial}_i \hat{\Phi}, \\ + (\hat{\psi}^{4+2A})^{R_0^2} \delta_{ij} \tilde{s}^i \tilde{s}^j, \\ \lambda := C + (\beta^y + \hat{\Omega} \hat{\phi}^y) \hat{\partial}_y \hat{\Phi}.$$

Evaluating either Eq. (94) or Eq. (95) at the three points given by (91)–(93) will produce a system of three equations in the three unknowns $\hat{\Omega}$, R_0 , and C ; the solution of the system will determine these constants. These unknowns are computed separately for the two stars, although they yield the same solution for the case of equal-mass binaries considered here. We also note that the star's surface remains fixed and the values of the specific enthalpy h at the three points (91)–(93) is unchanged, with $h = 1$ at (91) and (93).

C. Elliptic solver for the gravitational part

As discussed in detail in Refs. [73–75], Eqs. (11)–(13) are solved using the representation theorem of partial differential equations in a self-consistent way. Starting from

$$\nabla^2 f = S, \quad (96)$$

where S is a nonlinear function of f , and using the Green's function without boundary $G(x, x') = 1/|x - x'|$ that satisfies

$$\nabla^2 G(x, x') = -4\pi \delta(x - x'), \quad (97)$$

a solution for f is obtained as

$$f(x) = -\frac{1}{4\pi} \int_V G(x, x') S(x') d^3 x' + \frac{1}{4\pi} \int_{\partial V} [G(x, x') \nabla'^a f(x') - f(x') \nabla'^a G(x, x')] dS'_a. \quad (98)$$

where V is the domain of integration, $x, x' \in V \subseteq \Sigma_0$, the initial spacelike hypersurface. The volume V and its boundary ∂V depend on the coordinate system we are solving for, i.e., COCP or ARCP as described in Sec. III A. This is the principle of the KEH method [81] and will be suitably modified in order to account for the specific boundary conditions that exist in the new COCAL coordinate systems. For example, the conformal factor will be expressed as

$$\psi(x) = \chi(x) + \psi_{\text{INT}}(x), \quad (99)$$

where

$$\begin{aligned} \psi_{\text{INT}}(x) = & -\frac{1}{4\pi} \int_V \frac{S_{\psi}^g(x') + S_{\psi}^f(x')}{|x - x'|} d^3x' \\ & + \frac{1}{4\pi} \int_{\partial V} \left[\frac{\nabla'^a \psi(x')}{|x - x'|} - \psi(x') \nabla'^a \frac{1}{|x - x'|} \right] dS'_a, \end{aligned} \quad (100)$$

and

$$\begin{aligned} \chi(x) = & \frac{1}{4\pi} \int_{S_a \cup S_b} [G^{\text{BC}}(x, x') \nabla'^a (\psi_{\text{BC}} - \psi_{\text{INT}}(x')) \\ & - (\psi_{\text{BC}} - \psi_{\text{INT}})(x') \nabla'^a G^{\text{BC}}(x, x')] dS'_a. \end{aligned} \quad (101)$$

Note that G^{BC} is the Green's function associated with the boundary conditions applied on the corresponding field ψ_{BC} at the boundaries S_a and S_b . Formulas (99)–(101) will be applied separately on every coordinate patch. If, for example, we have one ARCP patch (as it happens in our computations) it means that the equations above will be applied three times: two for the COCP patches and one for the ARCP patch. Of course, the domains of integration vary according to the different patches considered. More specifically, if we denote by $B(R)$ a sphere of radius R in each of the COCP patch, then the integration domain of Eq. (100) will be $V = B(r_b) - B(r_e)$ and $\partial V = S_e \cup S_b = \partial B(r_e) \cup \partial B(r_b)$, while that of Eq. (101) will be $S_a \cup S_b = S_b$, since $r_a = 0$ for star configurations in the COCP patch. Similarly, in the ARCP patch the integration domain of Eq. (100) will be $V = B(r_b) - B(r_a)$, and that of Eq. (101) $\partial V = S_a \cup S_b$.

We recall that in Ref. [73] we have introduced a number of Green's functions $G^{\text{BC}}(x, x')$ suitable for various boundary conditions. Here we add one more Green's function used in the COCP patch

$$\begin{aligned} G^{\text{SD}}(x, x') := & \sum_{\ell=0}^{\infty} g_{\ell}^{\text{SD}}(r, r') \sum_{m=0}^{\ell} \epsilon_m \frac{(\ell - m)!}{(\ell + m)!} \\ & \times P_{\ell}^m(\cos \theta) P_{\ell}^m(\cos \theta') \cos[m(\phi - \phi')], \end{aligned} \quad (102)$$

where

$$g_{\ell}^{\text{SD}}(r, r') := \frac{r_{<}^{\ell}}{r_b^{\ell+1}} \left[\left(\frac{r_b}{r_{>}} \right)^{\ell+1} - \left(\frac{r_{>}}{r_b} \right)^{\ell} \right], \quad (103)$$

and $\epsilon_0 = 1$, $\epsilon_m = 2$ for $m \geq 1$, while P_{ℓ}^m are the associated Legendre polynomials, and $r_{>} := \sup\{r, r'\}$, $r_{<} := \inf\{r, r'\}$.

In the ARCP patch we use a Green's function $G^{\text{DD}}(x, x')$, whose radial part satisfies the Dirichlet-Dirichlet boundary conditions on S_a and S_b

$$\begin{aligned} g_{\ell}^{\text{DD}}(r, r') = & \left[1 - \left(\frac{r_a}{r_b} \right)^{2\ell+1} \right]^{-1} \frac{r_a^{\ell}}{r_b^{\ell+1}} \\ & \times \left[\left(\frac{r_{<}}{r_a} \right)^{\ell} - \left(\frac{r_a}{r_{<}} \right)^{\ell+1} \right] \left[\left(\frac{r_b}{r_{>}} \right)^{\ell+1} - \left(\frac{r_{>}}{r_b} \right)^{\ell} \right]. \end{aligned} \quad (104)$$

D. Elliptic solver for the fluid part

Next, we describe the method used to solve Eq. (57) and which is therefore valid only for the spinning binaries. The boundary condition for Φ , Eq. (58), is of von Neumann type, and therefore we could apply the Poisson solver of Sec. III C to obtain a solution. Instead, and as a demonstration of the versatility of the methods employed by COCAL, we will adapt the procedure discussed in Ref. [46] and solve this boundary-value problem as an application of the least-squares algorithm.

First, we assume that the solution of Eq. (57) can be written in the form

$$\Phi(x) = -\frac{1}{4\pi} \int_V \frac{S_{\Phi}(x')}{|x - x'|} dV + \zeta(x) = \Phi_V(x) + \zeta(x), \quad (105)$$

with $\zeta(x)$ obeying the Laplace equation

$$\nabla^2 \zeta(x) = 0. \quad (106)$$

Using the decomposition of Eq. (105), the boundary condition (58) is written as

$$\psi^A h u^t \omega^i m_i - m^i \partial_i \Phi_V - \psi^{A+A} \tilde{s}^i m_i = m^i \partial_i \zeta, \quad (107)$$

where we used the normal to the surface unit vector $m^i = (\hat{n}_s)^i$ instead of the gradient of the rest-mass density. The equation above is evaluated on the surface of the star, $R(\theta, \phi)$, and the velocity potential satisfies the following symmetries:

$$\Phi(r, \pi - \theta, \phi) = \Phi(r, \theta, \phi), \quad (108)$$

$$\Phi(r, \theta, 2\pi - \phi) = -\Phi(r, \theta, \phi), \quad (109)$$

which in turn imply that the homogeneous solution, which is regular at the stellar center, can be expanded as

$$\begin{aligned} \zeta(r, \theta, \phi) = & \sum_{\ell=1}^L \sum_{m=1}^{\ell} a_{\ell m} r^{\ell} \\ & \times [1 + (-1)^{\ell+m}] Y_{\ell}^m(\cos \theta) \sin(m\phi), \end{aligned} \quad (110)$$

where Y_{ℓ}^m are the spherical harmonics and $a_{\ell m}$ coefficients to be determined. When the spins of the stars are in arbitrary directions, the symmetries (108) and (109) no

longer apply and expression (110) will contain also cosine terms.

On the other hand, if $R(\theta, \phi)$ is the surface of the star, the spatial vector connecting any point on it with the center of coordinates is given by

$$\vec{x}(\theta, \phi) = R(\theta, \phi)(\sin \theta \cos \phi, \sin \theta \sin \phi, \cos \theta); \quad (111)$$

thus the unit normal vector will be

$$\hat{n}_s(\theta, \phi) := \left(\frac{\partial \vec{x}}{\partial \theta} \times \frac{\partial \vec{x}}{\partial \phi} \right) \left| \frac{\partial \vec{x}}{\partial \theta} \times \frac{\partial \vec{x}}{\partial \phi} \right|^{-1}, \quad (112)$$

or equivalently

$$\hat{n}_s = \frac{1}{\sqrt{h}} \left(\hat{r} - \frac{1}{R} \frac{\partial R}{\partial \theta} \hat{\theta} - \frac{1}{R \sin \theta} \frac{\partial R}{\partial \phi} \hat{\phi} \right), \quad (113)$$

where $\hat{r}, \hat{\theta}, \hat{\phi}$ are the spherical unit vectors and

$$h(\theta, \phi) := 1 + \left(\frac{1}{R} \frac{\partial R}{\partial \theta} \right)^2 + \left(\frac{1}{R \sin \theta} \frac{\partial R}{\partial \phi} \right)^2. \quad (114)$$

Using Eqs. (110) and (113), the boundary condition (107) is written as

$$\sum_{\ell=1}^L \sum_{m=1}^{\ell} a_{\ell m} F_{\ell m}(\theta, \phi) = H(\theta, \phi), \quad (115)$$

where

$$H(\theta, \phi) := \psi^4 h u^i \omega^i m_i - m^i \partial_i \Phi_V - \psi^{4+A} \bar{s}^i m_i, \quad (116)$$

and

$$F_{\ell m}(\theta, \phi) := [1 + (-1)^{\ell+m}] \times \left[\ell R^{\ell-1} Y_{\ell}^m \sin(m\phi) - \frac{\partial R}{\partial \theta} R^{\ell-2} \frac{\partial Y_{\ell}^m}{\partial \theta} \sin(m\phi) - \frac{\partial R}{\partial \phi} \frac{R^{\ell-2}}{\sin^2 \theta} Y_{\ell}^m m \cos(m\phi) \right]. \quad (117)$$

To solve for the coefficients $a_{\ell m}$, we consider the functional

$$\mathcal{E} := \sum_{\theta_i, \phi_j} \left[\sum_{\ell=1}^L \sum_{m=1}^{\ell} a_{\ell m} F_{\ell m}(\theta_i, \phi_j) - H(\theta_i, \phi_j) \right]^2 = 0, \quad (118)$$

of the discretized version of the boundary condition (115) and demand that for fixed indices p and q

$$\frac{\partial \mathcal{E}}{\partial a_{pq}} = 0. \quad (119)$$

The minimizing condition Eq. (119) then yields

$$\sum_{\ell, m} a_{\ell m} \left[\sum_{i, j} F_{\ell m}(\theta_i, \phi_j) F_{pq}(\theta_i, \phi_j) \right] \quad (120)$$

$$= \sum_{i, j} H(\theta_i, \phi_j) F_{pq}(\theta_i, \phi_j), \quad (121)$$

which is a linear system in terms of the $a_{\ell m}$ coefficients. For L even, the dimensions of the system is $M \times M$ with $M = L(L+1)/2$. After determining the coefficients $a_{\ell m}$, the solution for the velocity potential Φ is obtained from Eqs. (105) and (110).

IV. NUMERICAL RESULTS

In what follows we report tests of our new code against previous results obtained by other groups and then present some new ones. In particular, we focus on the construction of quasiequilibrium sequences for corotating, irrotational, and spinning binaries and produce a binary white dwarf solution (see Appendix D) in order to explore the weak-field limit of our code. We compute two main global-error indicators to measure the accuracy of our converged solutions; the first one is given by the relation $M_K = M_{\text{ADM}}$, where M_K and M_{ADM} are the Komar and Arnowitt-Deser-Misner (ADM) mass, respectively [107–111]. The second one is instead related to the first law of binary thermodynamics $dM_{\text{ADM}} = \Omega dJ$, where Ω is the orbital frequency and J the orbital angular momentum [93]. Explicit definitions and computational algorithms for these quantities within COCAL are presented in Appendix A.

Sequences of constant rest mass can be thought of as snapshots of an evolutionary process that drives the two stars close to each other as a result of gravitational radiation reaction. At every instant in time, the rest mass of each star is conserved; furthermore, if the flow is irrotational, the circulation of the fluid velocity on any loop is also conserved (Kelvin-Helmholtz theorem [36]). It is possible to characterize these sequences via the properties of the stars, such as the compactness or the ADM mass, when the binary has infinite separation and each star is spherical.

By varying the separation between the two stars and solving each time all the relevant equations, we obtain solutions of a given central rest-mass density, and then another loop of solutions has to be invoked in order to find the particular central rest-mass density that yields a star with the desired rest mass. Typically, this is done by a Newton-Raphson method, and it takes a maximum of ten iterations depending on the starting solution.

In this way we can monitor important quantities like the binding energy of the system, which is defined as

$$E_b := M_{\text{ADM}} - M_{\infty}, \quad (122)$$

and represents the total energy lost in gravitational waves by the system, since M_∞ is twice the ADM mass of a single isolated spherical star.

A. Corotating solutions

As mentioned in the Introduction, corotating states [106,112–114], i.e., states with zero angular velocity of

the star with respect to a corotating observer, probably are not physically realistic due to the low viscosity of the neutron-star matter. Such solutions represent an important step in the numerical solution of the binary problem, since they provide key insights for the numerical implementation of a stable algorithm. In particular, the surface-fitted coordinates, as well as the solution of the Euler integral, Eq. (32), can be thoroughly checked. This allows us to

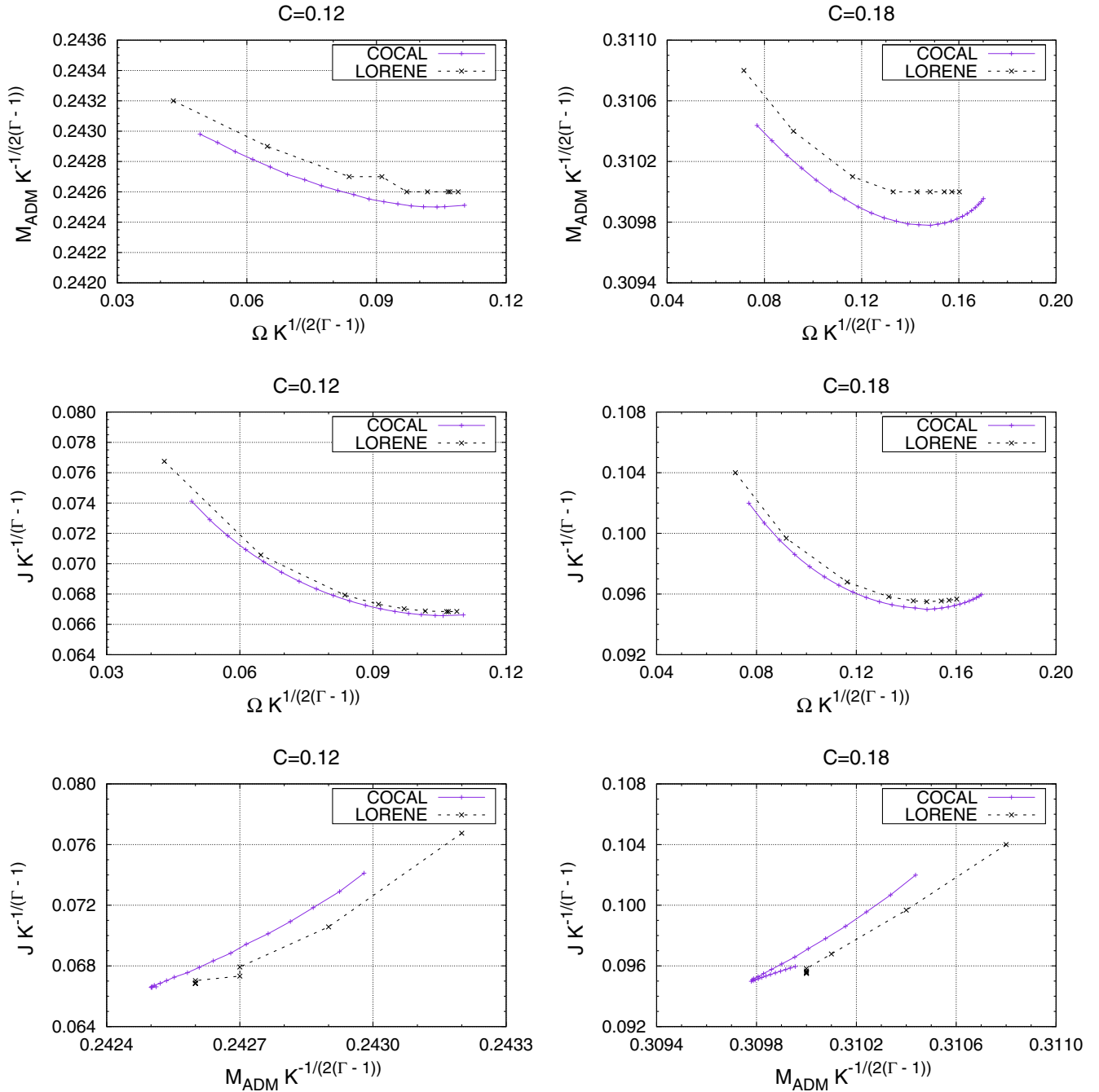


FIG. 2 (color online). Quasiequilibrium sequences for corotating binary neutron stars with EOS consisting of a single polytrope with $\Gamma = 2$. The left column corresponds to models with compactness $C = 0.12$, while the right column corresponds to $C = 0.18$. M and J are the total ADM mass and angular momentum of the system. The resolutions used are those given in Table II. A comparison is made with the results of Ref. [43], where similar solutions were obtained from the spectral code LORENE [115].

TABLE II. Grid parameters used for the corotating sequences of compactness 0.12, 0.18, presented in Fig. 2. Hs2d refers to solutions at large separations, while Hs2b refers to binaries with small separations. For the Hs2d case the separation between the two neutron stars is kept fixed at $d_s = 2r_c = 2.5$ while the surface of the neutron star (maximum value r_s) varies from $r_s = 0.5$ to $r_s = 0.86$ creating effectively binaries with separations from $5.0 = 2.5/0.5$ to $2.91 = 2.5/0.86$. Similarly in the Hs2b case $d_s = 2r_c = 2.125$, and the effective separations are from $2.125/0.74 = 2.87$ to $2.125/0.98 = 2.17$.

Type	Patch	r_a	r_s	r_b	r_c	r_e	N_r^f	N_r^l	N_r^m	N_r	N_θ	N_ϕ	L
Hs2d	COCP-1	0.0	var	10^2	1.25	1.125	50	64	80	192	48	48	12
	COCP-2	0.0	var	10^2	1.25	1.125	50	64	80	192	48	48	12
	ARCP	5.0	...	10^6	6.25	...	16	...	20	192	48	48	12
Hs2b	COCP-1	0.0	var	10^2	1.0625	1.03125	60	64	68	192	48	48	12
	COCP-2	0.0	var	10^2	1.0625	1.03125	60	64	68	192	48	48	12
	ARCP	5.0	...	10^6	6.25	...	16	...	20	192	48	48	12

perform a calibration without having to worry about the fluid flow (i.e., to solve the equation of conservation of rest mass). Corotating evolutionary configurations are known to exhibit a minimum in the mass and angular momentum versus the normalized angular velocity $\Omega K^{1/(2(\Gamma-1))}$, which was taken to denote the putative innermost stable circular orbit, beyond which the binary was thought to proceed rapidly toward a merger. In practice, fully general-relativistic simulations of inspiraling binary neutron stars do not show the existence of such an instability, revealing instead that the inspiral and merger is a smooth process [1,2]. Nevertheless, the presence of such a minimum represents a useful test of numerical codes, as does the appearance of a familiar spike, similar to the one encountered in binary black-hole solutions, when plotting the binding energy versus the angular momentum of the binary.

In Fig. 2 we present sequences of binary neutron stars that correspond to the compactness of $C := M_{\text{ADM}}/R = 0.12$ and 0.18, where M_{ADM} and R are the (ADM) mass and radius of each star when taken at infinite separation. The ADM and Komar mass, as well as other quantities used in COCAL, are described in detail in Appendix A. The adiabatic index is $\Gamma = 2$, and the polytropic constant is set to be $K = 1$. In the various plots a comparison is made between the results obtained with COCAL and those presented in Ref. [43], where the same initial data were computed using LORENE, a pseudospectral code developed by the Meudon group [43]. As we can see, the relative difference in the results between the two codes is of the order of 0.05%, even when a medium resolution is used for COCAL. The grid structure used in these calculations is the one described in Table II.

Similarly, in Fig. 3 we report the change in the central rest-mass density with respect to the one at infinity, which is $\rho_\infty = 0.0922$ for compactness $C = 0.12$, while it is $\rho_\infty = 0.1956$ for $C = 0.18$. Clearly, the central rest-mass density decreases as the binary comes closer, making the onset of an instability to gravitational collapse very unlikely [116]. In addition, as a measure of accuracy of

these corotating sequences, we plot in Fig. 4 the relative difference

$$\Delta_M := \left| \frac{M_{\text{ADM}} - M_{\text{K}}}{M_{\text{ADM}}} \right|, \quad (123)$$

as a function of the binary separation d_s/r_s . Note that all radii are here normalized to the scaling factor R_0 and are therefore dimensionless, so that, e.g., the physical distance between the two neutron stars is $d_s R_0$. As we can see, even for the medium resolution used in these calculations the error is below 10^{-4} . All of the quantities in the expression above have been extracted from the ARCP patch, as integrals at infinity. We note that at present COCAL does not implement a unifying mesh, and this prevents us from calculating the virial error as obtained by Friedman, Uryu, and Shibata [93], since we are using overlapping coordinate systems. We plan to revisit this issue in the future.

Finally, in Fig. 5 we report sequences of corotating binaries for increasing central rest-mass density at different separations, from $d_s/R_0 = 4$, down to separation in which

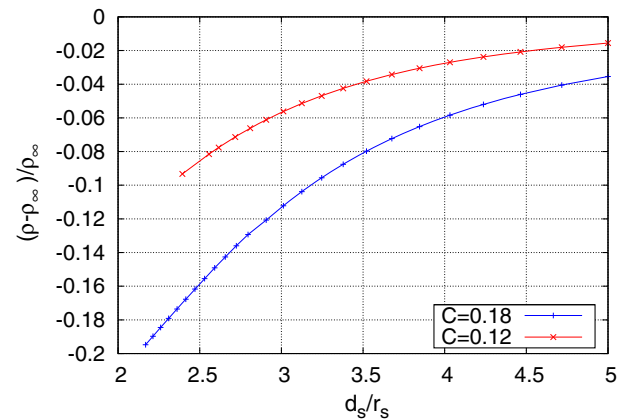


FIG. 3 (color online). Relative change in the central rest-mass density for the corotating sequences in Fig. 2, shown as a function of separation.

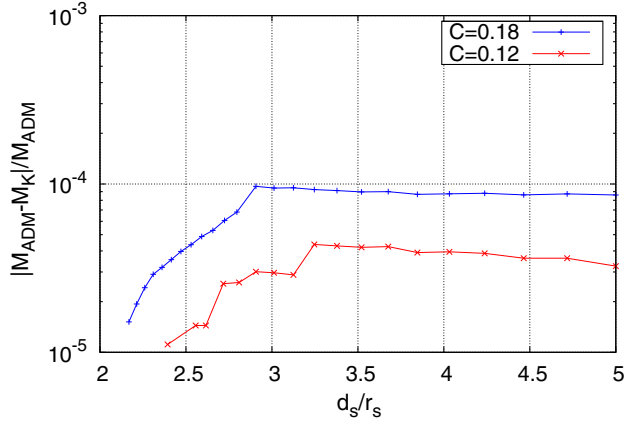


FIG. 4 (color online). Measure of the virial error $M_K = M_{ADM}$ for the corotating sequences in Fig. 2, as a function of separation.

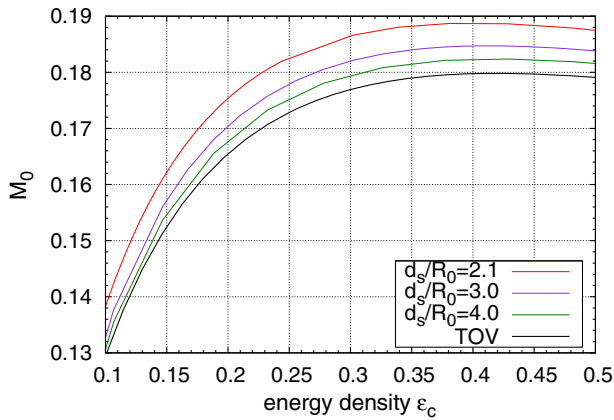


FIG. 5 (color online). Corotating sequences versus central energy density for different separations. The TOV curve corresponds to infinite separation. Here we use $r_s = 1$, and therefore R_0 is the radius of the star.

the two stars are almost touching $d_s/R_0 = 2.125$. Here we use $r_s = 1$, and therefore the radius of the neutron star is R_0 . Clearly, for any given central energy density a larger mass is supported by the binary (supramassive solutions) when we move to closer configurations, once again excluding the onset of an instability to gravitational collapse to black hole [117–119].

B. Irrotational sequences

As anticipated in the Introduction, irrotational neutron stars have been considered as a reasonable first approximation to describe the flow in binary configurations. In such a case, the total angular momentum is less than the corresponding of a corotating binary, since in each star there is a flow in the counterdirection with respect to the orbital motion.⁸ This has two consequences. First the

⁸For this reason these binaries are also called *counter-rotating configurations*.

inspiral of irrotational binaries is faster than that of corotating ones or, equivalently, the gravitational-wave frequency is expected to increase with a faster rate for irrotational systems. To first order in the spins, the rate of inspiral is [120,121]

$$\frac{dr}{dt} = -\frac{64}{5}\nu\left(\frac{M}{r}\right)^3\left\{1 - \frac{7}{12}\frac{1}{M^2}\left(\frac{M}{r}\right)^{3/2}\right. \\ \left.\times \hat{\mathbf{L}} \cdot \left[\left(19 + 15\frac{M_2}{M_1}\right)\vec{\mathcal{S}}_1 + \left(19 + 15\frac{M_1}{M_2}\right)\vec{\mathcal{S}}_2\right]\right\}, \quad (124)$$

where ν is the symmetric mass ratio and $\hat{\mathbf{L}}$ the unit angular momentum vector. From (124) we can see that

$$|j^{\text{irr}}| > |j^{\text{cor}}|, \quad (125)$$

which is expected, since spinning binaries have to radiate also the additional angular momentum before they merge [122].

Second, in the light of the results obtained for binary black holes, where binaries with larger spins lead to increasingly spinning final black holes [123,124], the irrotational binary system will eventually lead to a Kerr black hole that is more slowly rotating than the corresponding one produced by the corotating binary.

As done in Sec. IV A for corotating binaries, we compare in Fig. 6 our irrotational solutions for compactness $\mathcal{C} = 0.12$ and 0.18 against the corresponding results presented in Ref. [43]. Although we use here a relatively small resolution, i.e., Hs2d from Table II, the relative difference with Ref. [43] is again of the order of 0.05%. Note that for binaries with compactness $\mathcal{C} = 0.12$, the variable r_s ranges from $r_s = 0.5$ to $r_s = 0.87$, which corresponds to coordinate separations $d_s/r_s = 2.5/0.5 = 5$ and $d_s/r_s = 2.5/0.87 = 2.87$, respectively. On the other hand, for $\mathcal{C} = 0.18$, r_s varies from $r_s = 0.5$ to $r_s = 0.79$, which corresponds to separations from $d_s/r_s = 5$ to $d_s/r_s = 3.16$, respectively. Note also that the minimum in these plots marks the mass-shedding limit and the creation on the equatorial plane of a cusp in the rest-mass density.

In Fig. 7 we present the results relative to the irrotational binary solutions with $r_s = 0.76$ and compactness $\mathcal{C} = 0.18$. More specifically, in the left column we report the contour plots of the conformal factor ψ from 1.0 to 1.33 with step 0.01, of the rest-mass density from 0.0 to 0.3 with step 0.01, and of the velocity potential Φ from -0.2 to 0.2 with step 0.01, all on the (x, y) plane. On the other hand, in the right column we show the shift and the fluid velocity vector fields on the (x, y) plane, and a contour plot of the rest-mass density on the (y, z) plane.

Similarly, in Fig. 8 we report two global error indicators computed for irrotational binaries with compactness

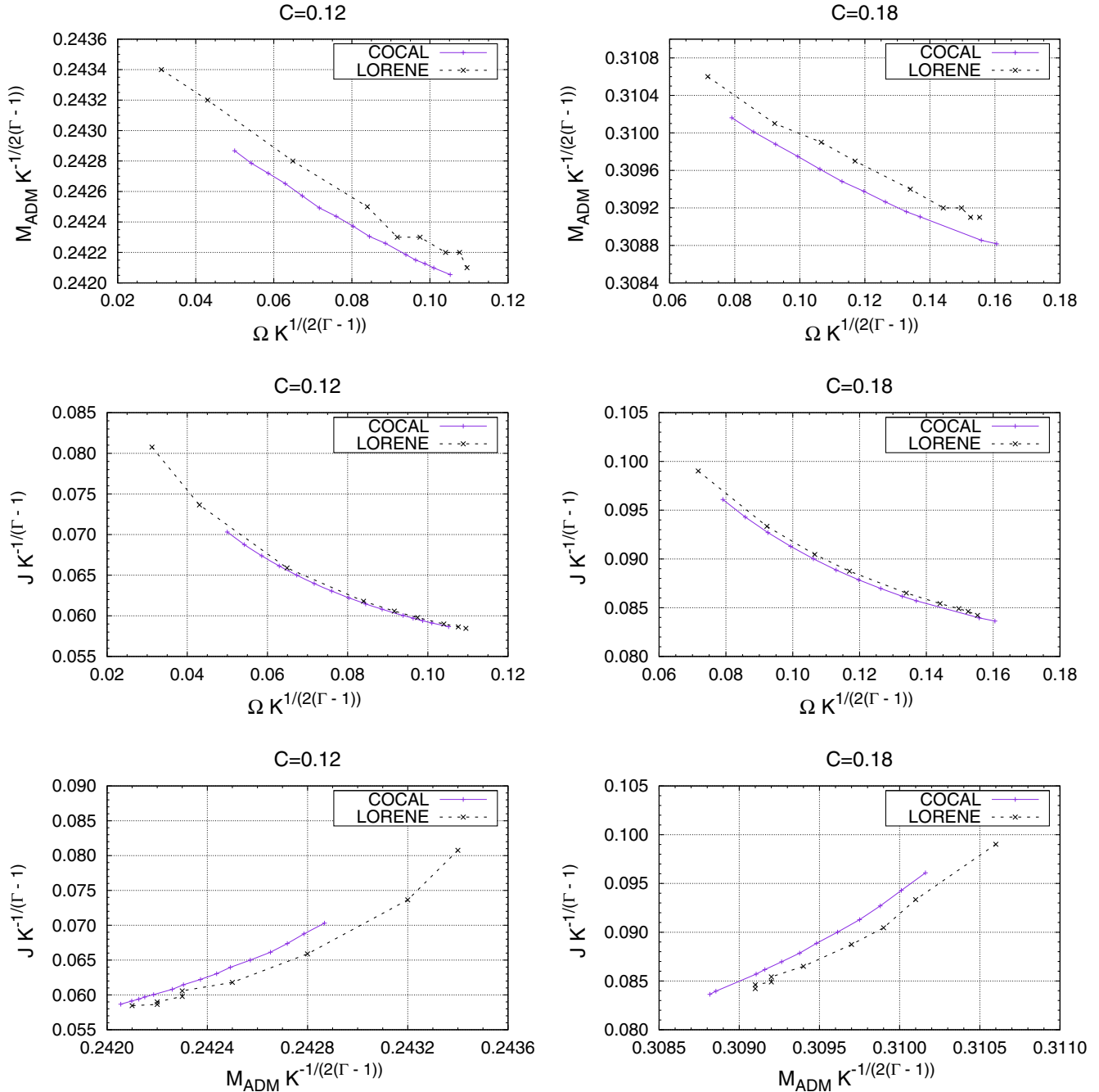


FIG. 6 (color online). Sequences of irrotational binary neutron stars, with an EOS consisting of a single polytrope with $\Gamma = 2$. The left column corresponds to models with compactness $C = 0.12$, while the right column corresponds to $C = 0.18$. The resolution is Hs2d from Table II. A comparison is made with the results presented in [43], where similar solutions were obtained from the spectral code LORENE [115].

$C = 0.18$. More specifically, the top panel shows the fractional difference in the Komar and ADM masses, while the bottom panel shows the fractional error of the $dM_{\text{ADM}} = \Omega dJ$ relation; note that the latter is a rather stringent test and that a fractional error below 0.7% gives us confidence on the accuracy of our solutions already at an intermediate resolution. Finally, in Fig. 9 we plot the

relative change in the central rest-mass density as the coordinate separation between the two stars is reduced. This figure should be compared with the corresponding Fig. 3 for corotating binaries and shows that again the central rest-mass density decreases as the two stars approach, but also that this decrease is smaller, of 1 order of magnitude or more, than in the corotating case.

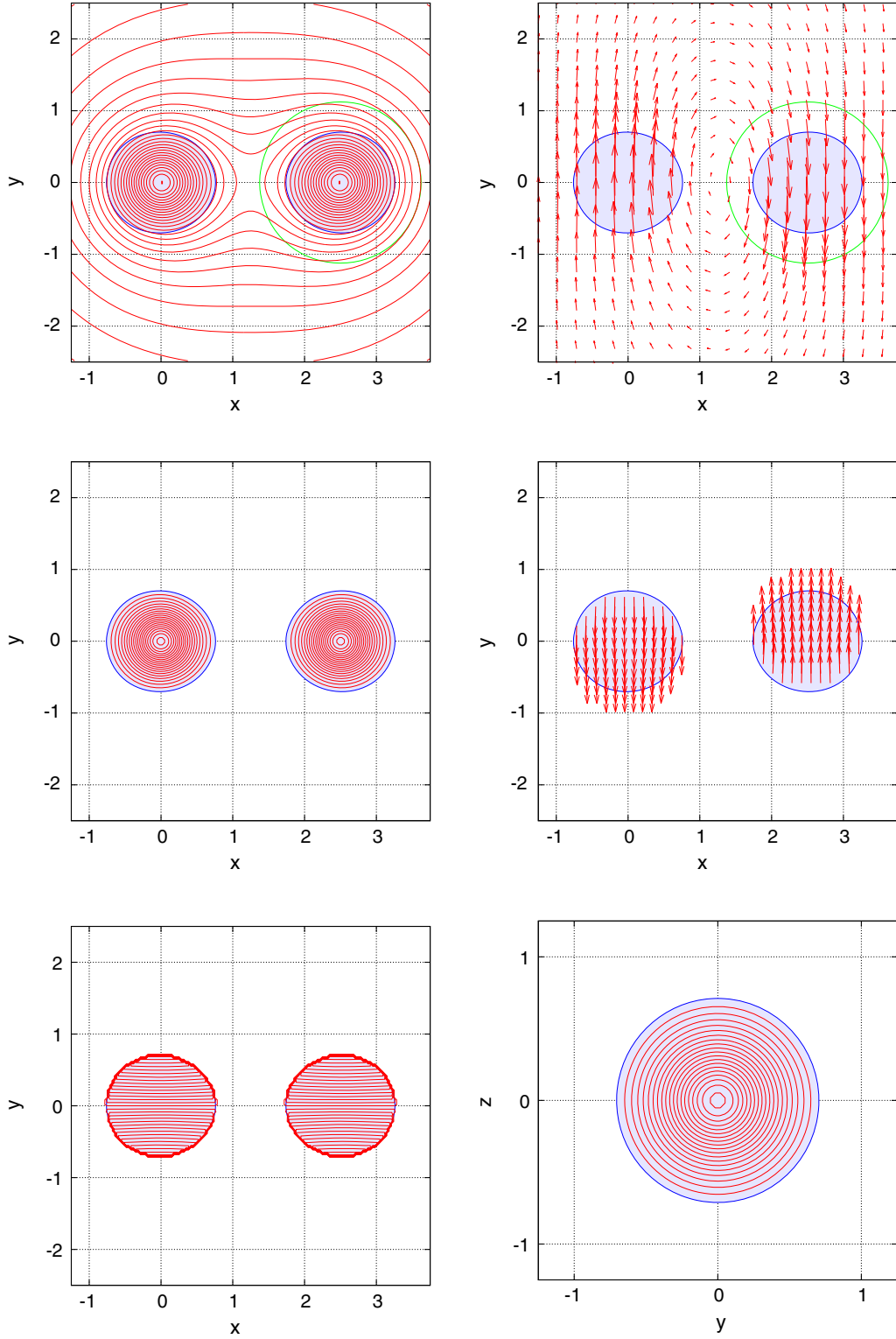


FIG. 7 (color online). Irrotational binary solution with $r_s = 0.76$ and compactness $\mathcal{C} = 0.18$. The separation between the two neutron stars is $d_s/r_s = 2.5/0.76 = 3.29$. Left column: contour plots of the conformal factor ψ from 1.0 to 1.33 with step 0.01, of the rest-mass density from 0 to 0.3 with step 0.01, and of the velocity potential Φ from -0.2 to 0.2 with step 0.01, all on the (x, y) plane. Right column: shift and fluid velocity vector fields on the (x, y) plane, and contour plot of the rest-mass density on the (y, z) plane. Note that the green sphere corresponds to the excised sphere S_e of COCP-1.

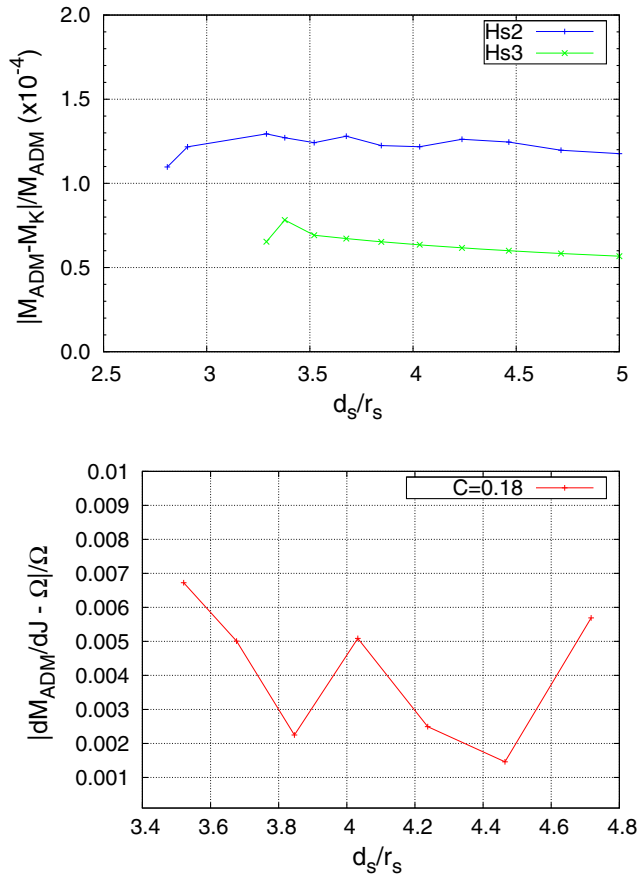


FIG. 8 (color online). Top panel: relative error in the relation $M_K = M_{\text{ADM}}$ for irrotational sequences with $C = 0.18$ using the Hs2d grid of Table II and the Hs3d grid of Table III. Bottom panel: relative error in the relation $dM_{\text{ADM}} = \Omega dJ$ for the irrotational sequences of compactness $C = 0.18$ as a function of the coordinate separation d_s/r_s .

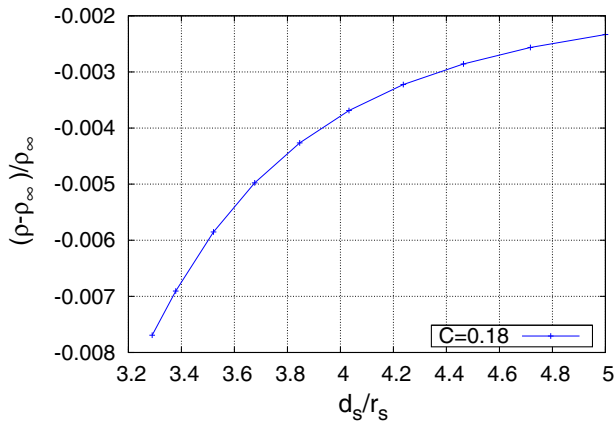


FIG. 9 (color online). Relative change in the central rest-mass density for the irrotational sequences with $C = 0.18$ of Fig. 6 as a function of separation. Note that the decrease as the stars approach each other is 1 order of magnitude (or more) smaller than for corotating binaries (cf. Fig. 3).

TABLE III. Grid parameters used for the irrotational solution of compactness $C = 0.18$, presented in Fig. 7. The separation between the two neutron stars is $d_s/r_s = 2.5/0.76 = 3.29$.

Type	Patch	r_a	r_s	r_b	r_c	r_e	N_r^i	N_r^1	N_r^m	N_r	N_θ	N_ϕ	L
Hs3d	COCP-1	0.0	0.76	10^2	1.25	1.125	100	128	160	384	96	96	12
	COCP-2	0.0	0.76	10^2	1.25	1.125	100	128	160	384	96	96	12
	ARCP	5.0	...	10^6	6.25	...	32	...	40	384	96	96	12

C. Spinning sequences

We conclude our discussion of the results with the new COCAL by presenting our first calculations of quasiequilibrium binary systems of spinning neutron stars. The neutron-star matter is modeled using a piecewise polytrope representation of the APR1 EOS [104]. As mentioned in Sec. II C, an EOS with N polytropic segments requires $2N$ parameters to be specified, which can be thought of as one adiabatic constant, $N - 1$ dividing rest-mass densities, and N adiabatic indices. In Ref. [101] it was found that a number of tabulated nuclear matter EOS can be modeled with three segments above nuclear density and one in the crust, thus with a total of four polytropic zones. The error in the approximation is $\sim 0.1\%$, or at worst $\sim 4\%$. A fit with a minimum error was described in [101] that had a fixed crust with $\Gamma_0 = 1.35692$, $K_0 = 3.59389 \times 10^{13}$, and three core zones with adiabatic exponents $\{\Gamma_1, \Gamma_2, \Gamma_3\}$, joining the different pieces at rest-mass densities $\rho_1 = 10^{14.7} \text{ gr/cm}^3$ and $\rho_2 = 10^{15} \text{ gr/cm}^3$. Additional information on the properties of the initial data are collected in Table IV.

The spin contribution to the fluid velocity is expressed through the spatial three-vector \tilde{s}^i [cf. Eq. (56)], which we express as

$$\tilde{s}^i = \tilde{S}_0(-y, x, 0), \quad (126)$$

where the Cartesian coordinates x, y are centered in the COCP patch, and the positive (negative) constant \tilde{S}_0 denotes the magnitude of corotation (counterrotation).

In Table IV we report the properties of a sequence of binary neutron stars with constant rest mass $M_0 = 1.5388M_\odot$, corresponding to an ADM mass $M_{\text{ADM}} = 1.35M_\odot$ when the stars are at infinite separation. The freedom in the choice of the spin velocity vector defined in Eqs. (56) and (126) has been fixed by taking $A = 0$, while for \tilde{S}_0 we examine two cases: $\tilde{S}_0 = 0.01$, which corresponds to a spinning period of ~ 3 ms, and $\tilde{S}_0 = 0.05$, which corresponds to the extreme case of a period ~ 0.6 ms. These choices correspond to spinning periods that are more than twice smaller than those considered in [70], where the maximum value considered was 6.7 ms. Although it is rather unlikely that such small rotation periods are encountered in reality in binaries about to merge, it is a good consistency check for our new code and an exploration of its limits.

TABLE IV. Top part: summary of the parameters in the piecewise polytropic EOS used to represent the APR1 EOS. Bottom part: the first lines report the main properties of the maximum-mass nonrotating configuration of the APR1 EOS; the second line reports the properties of the nonrotating configuration used to construct the constant rest-mass and spinning binary sequences computed in Sec. IV C. The last four lines report the stellar properties for the binary in the sequence having the smallest separation, with the last column providing a possible estimate of the maximum absolute contribution of the spin angular momentum, $(J_{\text{sp}} - J_{\text{ir}})/2$.

$\log p_1$	Γ_0	Γ_1	Γ_2	Γ_3	$\log \rho_0$	$\log \rho_1$	$\log \rho_2$	\tilde{S}_0	A	$(J_{\text{sp}} - J_{\text{ir}})/2$
33.943	1.357	2.442	3.256	2.908	14.294	14.700	15.000
$M_{\text{ADM}}[M_\odot]$	$M_0[M_\odot]$	$M_p[M_\odot]$	$R[\text{km}]$	M_{ADM}/R	$\log \rho_c$	$\log p_c$	$\log e_c$	\tilde{S}_0	A	$(J_{\text{sp}} - J_{\text{ir}})/2$
1.666	1.989	2.294	7.995	0.307	15.489	36.340	15.642
1.350	1.539	1.636	9.138	0.218	15.221	35.562	15.276
2.661	1.539	1.636	10.246	...	15.220	35.559	15.275	0.01	0	0.0225
2.661	1.539	1.636	10.249	...	15.220	35.560	15.275	0.01	-6	0.0062
2.661	1.539	1.636	10.260	...	15.218	35.556	15.274	0.05	0	0.1176
2.661	1.539	1.636	10.248	...	15.219	35.559	15.275	0.05	-6	0.0313

The top left panel of Fig. 10 reports the dimensionless binding energy E_b/M_∞ of the binary as a function of the dimensionless orbital frequency ΩM_∞ . Considered and compared are an irrotational binary (violet solid line) and two spinning binaries, one with $\tilde{S}_0 = 0.01$ (red solid line) and another one with $\tilde{S}_0 = 0.05$ (blue solid line). All binaries are modeled with the APR1 EOS using the grid parameters of Table V, and both of the spinning binaries have a velocity field with $A = 0$. Also shown for comparison is the irrotational fourth post-Newtonian (4PN) (black dashed line) as well as the third post-Newtonian (3PN) corotating (green dotted line) approximation [125–128]. Explicit forms for these curves are given in

Appendix E. In the top right panel of Fig. 10 we report instead the analogue curves for the dimensionless angular momentum J/M_∞^2 .

We also note that a closer comparison with a PN expression for spinning neutron stars would be interesting. At the same time, it involves a number of subtleties. In fact, in order to correctly plot such PN spinning curves it is necessary to take into account two different effects. First, at each separation (orbital frequency) the PN expressions should use the correct values of the spins, which we recall increase (in our case approximately linearly) along the constant rest-mass sequence. This is made difficult by the fact that these spins cannot be measured separately in our

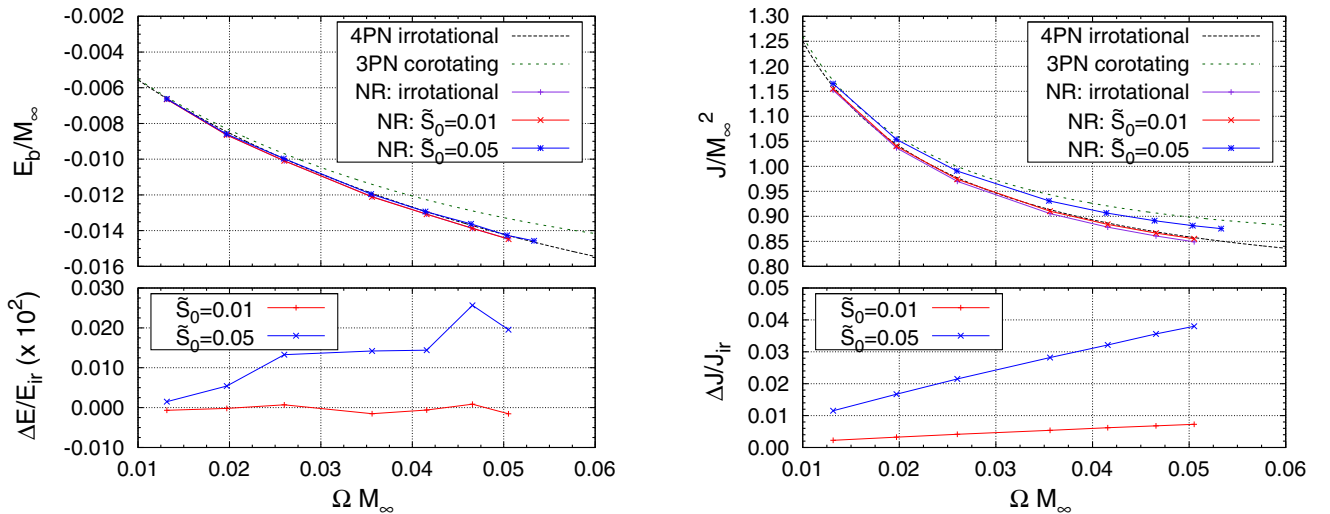


FIG. 10 (color online). Top: dimensionless binding energy (left panel) and angular momentum (right panel) as a function of the dimensionless orbital frequency for sequences of constant rest mass neutron-star binaries with $M_0 = 1.5388M_\odot$. Shown with different lines are an irrotational sequence (violet solid line) and two spinning ones with $A = 0$ and either $\tilde{S}_0 = 0.01$ (red solid line) or $\tilde{S}_0 = 0.05$ (blue solid line). All binaries are modeled with the APR1 EOS and are also shown for comparison is the 4PN irrotational (black dashed line), and the 3PN corotating (green dotted line) approximation. Bottom: Fractional differences of the $\tilde{S}_0 = 0.01$ and $\tilde{S}_0 = 0.05$ spinning sequences with respect to the irrotational sequence, $\Delta E/E_{\text{ir}} := E_{\text{sp}}/E_{\text{ir}} - 1$, $\Delta J/J_{\text{ir}} := J_{\text{sp}}/J_{\text{ir}} - 1$.

approach as they are part of the global solution. These additional terms for aligned spins will typically move the binding energy to more negative values relative to the irrotational curve. Second, the masses appearing in the PN expression need to be modified to account for the spin kinetic energy. In contrast to binary black holes, where it is possible to distinguish the irreducible mass from the spin-induced mass [125–128], accounting for this contribution is not easy for neutron stars. However, what is important here is that these terms are positive and will move the quasiequilibrium curve upwards relative to the irrotational curve and toward the corotating solution.

This is indeed the behavior that is shown by our solutions, which fall between the irrotational sequence and the corotating sequence; furthermore, the use of larger initial spins yields binding energies that are systematically larger as part of the orbital kinetic energy is channeled into “spinning-up” the stars. Clearly, the differences in the binding energy with respect to the irrotational binaries are very small even for these high spinning rates, with a maximum of 0.03% as it can be seen in the bottom left panel of Fig. 10. More pronounced are the differences for the angular momentum which are depicted on the bottom right panel of Fig. 10 with a maximum of 4%. Note also that the sign of \tilde{S}_0 determines the relative position of the spinning sequence relative to the irrotational one. In particular, with a negative value for \tilde{S}_0 , the angular-momentum curve for the spinning sequence would have appeared below the irrotational one.

Finally, in Fig. 11 we report an estimate of the spin contribution to the total angular momentum for a different value of A . For the same binaries presented in Fig. 10 the relative difference between the angular momentum of the

spinning binaries, J_{sp} , and that of an irrotational binary, J_{ir} with $A = -6$ is at most 1% of the total, smaller than the 4% value obtained with $A = 0$ of Fig. 10. Note that this quantity is not expected to be constant along this sequence, where only the rest mass and the spinning coefficient \tilde{S}_0 are kept constant.

If we estimate the dimensionless spin angular momentum to be

$$\chi := \frac{S}{M_{\text{ADM}}^2} := \frac{1}{2} \left(\frac{J_{\text{sp}} - J_{\text{ir}}}{M_{\text{ADM}}^2} \right), \quad (127)$$

then because the ADM mass of the spinning binaries is very close to the irrotational one and lies in the range $M_{\text{ADM}} \in [1.33, 1.34]$, the dimensionless spin takes values in the range $\chi \in [0.027, 0.066]$ for the case with $A = 0$ and $\tilde{S}_0 = 0.05$, and values in the range $\chi \in [0.0017, 0.0035]$ for the $A = -6$, $\tilde{S}_0 = 0.01$ case. In all the cases considered we have found that the error estimates discussed in the previous sections lead quite generically to relative errors that are $\lesssim 0.7\%$, and that smaller errors can be obtained with grids having a higher resolution.

V. CONCLUSION

We have presented the extension of the COCAL code to treat binary configurations of compact stars within the IWM formalism of general relativity. As with the work done for binary black holes, we have used multiple coordinate patches so as to be able to treat asymmetric binaries. Also in the spirit of previous work, we have introduced a particular normalization scheme that allows us to accurately compute binary systems that have small or large separations, recovering the spherical limit at large distances. This is done by keeping the stars at fixed coordinate positions, but artificially reducing their radius. Furthermore, we have made use of surface-fitted coordinates to describe accurately the stellar shape as it varies along sequences of constant rest mass.

Also for the nonvacuum spacetimes considered here, we have employed the KEH method [76–81], in which the gravitational equations are solved using Poisson solvers with appropriate Green’s functions, while for the conservation of rest mass we employ a least-squared algorithm. The code makes use of a piecewise polytropic description to represent the EOS of stellar matter and, for the specific cases considered here, we have adopted the representation of the APR1 EOS [104].

Making use of a suitably adapted formulation described in Ref. [63], the code is able to describe fluid flows within the stars that corresponds to corotating, irrotational, but also spinning binaries. As a validation of the numerical solutions, we have constructed a number of sequences of corotating and irrotational binary neutron stars having the same mass. The results for corotating and irrotational

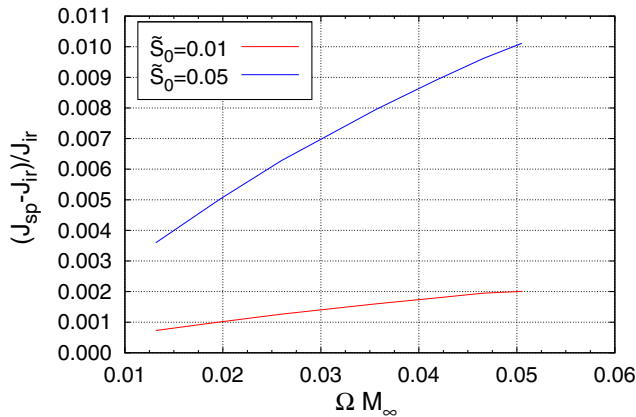


FIG. 11 (color online). Spin contribution to the total angular momentum. Shown for the same binaries presented in Fig. 10 but with $A = -6$ is the relative difference between the angular momentum of the spinning binaries and that of an irrotational binary. Note that despite the short spin periods considered, the contribution of the spin angular momentum is at most 1% of the total, smaller than the $A = 0$ case Fig. 10, where the same contribution was close to 4%.

binaries have been compared with those published from the pseudospectral code LORENE [43], and they revealed that the relative difference in the results between the two codes is of the order of 0.05%, even when a medium resolution is used for COCAL.

When considering spinning binaries, and although the code can handle arbitrary rotation prescriptions for the individual stars, we have concentrated here on the case of fluid flows in which the spins are parallel to the orbital angular momentum. For this class of solutions, and to explore the possible range of behaviors, we have considered sequences with stars that either are slowly spinning or are spinning at rates that are 10 times larger than those observed in binary pulsars systems. In all the cases considered, we have found that error estimates of different types lead to relative errors that are $\lesssim 0.7\%$.

A number of applications of these results and of additional developments of the code are expected to take place in the coming months. First, we will explore the impacts of stellar spins in numerical simulations of binary neutron stars; more specifically, by exploiting the high convergence order of our new numerical general-relativistic code [129], we plan to extend the work carried out in [130] for the inspiral part and the one recently published in [29,33] for the postmerger signal. Second, by combining the approaches followed in the solution of binary black holes and binary neutron stars, we will extend the code to handle also binaries comprising a black hole and a neutron star of different masses and spin orientation. Third, we will explore the space of solutions in which the spins of the neutron stars are oriented arbitrarily as these are likely to correspond to the most realistic configurations. Finally, working on a parallelization of the code will allow us to obtain results with much smaller computational costs, enabling us to provide public initial data for spinning binary neutron stars under a variety of conditions.

ACKNOWLEDGMENTS

We thank John Friedman for carefully reading the manuscript and providing useful input. We also thank Luc Blanchet, Alejandro Bohé, and Gerhard Schäfer for useful discussions regarding the post-Newtonian approximation. Partial support comes from the DFG Grant No. SFB/Transregio 7 and by “NewCompStar,” COST Action MP1304. A.T. is supported by the LOEWE-Program in HIC for FAIR. This work was supported by JSPS Grant-in-Aid for Scientific Research (C) 23540314, 15K05085, and 25400262.

APPENDIX A: MASS AND ANGULAR MOMENTUM

In this appendix we review the mathematical definitions of several of the quantities that have been used to characterize the properties of the binaries. We start with the rest mass

of each star, M_0 , defined as an integral over the spacelike hypersurface Σ_t of the rest-mass density as measured by the comoving observers

$$\begin{aligned} M_0 &:= \int_{\Sigma_t} \rho u^\alpha dS_\alpha = \int_{\Sigma_t} \rho u^\alpha \nabla_\alpha t \sqrt{-g} d^3x \\ &= \int_{\Sigma_t} \rho u^t \alpha \psi^6 r^2 \sin \theta dr d\theta d\phi. \end{aligned} \quad (\text{A1})$$

In COCAL, integrals like this are computed in dimensionless form using normalized coordinates. With the help of Eq. (66), Eq. (A1) is rewritten as

$$\hat{M}_0 := R_0^3 \int_{\Sigma_t} K_i^{1/(1-\Gamma_i)} q^{1/(\Gamma_i-1)} u^t \alpha \psi^6 \hat{r}^2 \sin \theta d\hat{r} d\theta d\phi, \quad (\text{A2})$$

where K_i depends on \hat{r} . The integrand in Eq. (A2) is evaluated on the gravitational coordinates; therefore an interpolation to the surface-fitted coordinates is needed before the integral evaluation.

Next, a measure of the total energy of the system is given by the ADM mass, M_{ADM} , which is defined as a surface integral at spatial infinity as

$$\begin{aligned} M_{\text{ADM}} &:= \frac{1}{16\pi} \int_\infty (f^{im} f^{jn} - f^{ij} f^{mn}) \partial_j \gamma_{mn} dS_i \\ &= -\frac{1}{2\pi} \int_\infty \partial^i \psi dS_i = -\frac{1}{2\pi} \int_\infty \frac{\partial \psi}{\partial r} r^2 \sin \theta d\theta d\phi, \end{aligned} \quad (\text{A3})$$

and which in normalized coordinates becomes

$$\hat{M}_{\text{ADM}} := -R_0 \frac{1}{2\pi} \int_{r=r_b} \frac{\partial \psi}{\partial \hat{r}} \hat{r}^2 \sin \theta d\theta d\phi. \quad (\text{A4})$$

Note that spatial infinity in COCAL is represented by a spherical surface with radius $r \approx 0.8r_b$ of the ARCP coordinate patch. Closely related to the ADM is the Komar mass of the binary, which is related to the timelike Killing field t^α and is defined as

$$M_{\text{K}} := -\frac{1}{4\pi} \int_\infty \nabla^\alpha t^\beta dS_{\alpha\beta} = \frac{1}{4\pi} \int_\infty \partial^\alpha dS_\alpha, \quad (\text{A5})$$

or in normalized form as

$$\hat{M}_{\text{K}} := R_0 \frac{1}{4\pi} \int_{r=r_b} \frac{\partial \alpha}{\partial \hat{r}} \hat{r}^2 \sin \theta d\theta d\phi. \quad (\text{A6})$$

The angular momentum of the system is also calculated from a surface integral at spatial infinity

$$J := \frac{1}{8\pi} \int_{\infty} K_j^i \phi^j dS_i = \frac{1}{8\pi} \int_{\infty} A_{ij} \phi^j x^i r_{\infty} \sin \theta d\theta d\phi, \quad (\text{A7})$$

where ϕ^i is the generator of the orbital trajectories and we have used the maximal slicing gauge. The corresponding normalized quantity is

$$\hat{J} := R_0^2 \frac{1}{8\pi} \int_{r=r_b} \hat{A}_{ij} \hat{\phi}^j \hat{x}^i \hat{r}_b \sin \theta d\theta d\phi. \quad (\text{A8})$$

Finally, we also compute the ‘‘proper mass’’ of each star as the integral of the total energy density measured by the comoving observer

$$M_p := \int_{\text{star}} \epsilon u^{\alpha} dS_{\alpha}. \quad (\text{A9})$$

APPENDIX B: ISOTROPIC COORDINATES TOV SOLVER

In this appendix we describe our implementation for obtaining spherical solutions and the related rescaling that is used in COCAL. We can obtain the same solutions using a one-dimensional KEH solver that mimics the full three-dimensional code in a 3 + 1 setting. However, because most of the time the TOV equations are presented in terms of Schwarzschild coordinates while the actual calculations are performed in isotropic coordinates, in what follows we show how to transform the system of equations from Schwarzschild to isotropic coordinates without having to go through a new derivation of equations and automatically obtaining a smooth solution at the stellar surface. The results are of course identical to machine precision, at least for simple polytropes we have checked. To the best of our knowledge this approach has not been presented before in the literature.

We recall that the line element in Schwarzschild and in isotropic coordinates is given, respectively, by

$$ds^2 = -A(r)dt^2 + B(r)dr^2 + r^2 d\Omega^2, \quad (\text{B1})$$

$$= -\alpha^2(\bar{r})dt^2 + \psi^4(\bar{r})(d\bar{r}^2 + \bar{r}^2 d\Omega^2), \quad (\text{B2})$$

with well known expressions for the functions $A(r)$, $B(r)$, $\alpha(\bar{r})$, $\psi(\bar{r})$ for the exterior of the star. For the interior, instead, we need to solve the TOV equations

$$\frac{dA}{dr} = -\frac{2A}{\epsilon + p} \frac{dp}{dr}, \quad (\text{B3})$$

$$\frac{dp}{dr} = -\frac{(\epsilon + p)(m + 4\pi r^3 p)}{r^2 - 2mr}, \quad (\text{B4})$$

where

$$\frac{dm}{dr} = 4\pi r^2 \epsilon, \quad \text{and} \quad B(r) = \frac{1}{1 - 2m(r)/r}. \quad (\text{B5})$$

Of course, it not difficult to derive the TOV equations in the isotropic coordinates (B2) and then perform a direct numerical integration in these coordinates. However, this is not necessary, and it is possible to always work in Schwarzschild coordinates rescaling the radial profile of the solution so as to make the surface of the star appear at the correct position and automatically obtain a smooth solution in $[0, \infty)$ without resorting to a postprocessing rescaling.

Comparing Eqs. (B1) and (B2) it is easy to deduce that

$$\psi^2(\bar{r})d\bar{r} = \sqrt{B}dr \quad \text{and} \quad \psi^2(\bar{r})\bar{r} = r, \quad (\text{B6})$$

which yield

$$\frac{dr}{d\bar{r}} = \frac{r}{\bar{r}} \sqrt{1 - \frac{2m(r)}{r}}. \quad (\text{B7})$$

Using Eq. (B7), we can rewrite the TOV system in terms of the isotropic radial coordinate \bar{r} as

$$\frac{dm}{d\bar{r}} = (4\pi r^2 \epsilon) \frac{r}{\bar{r}} \sqrt{1 - \frac{2m}{r}}, \quad (\text{B8})$$

$$\frac{dp}{d\bar{r}} = -\frac{(\epsilon + p)(m + 4\pi r^3 p)}{\sqrt{1 - 2m/r}} \frac{1}{r\bar{r}}, \quad (\text{B9})$$

$$\frac{d\psi}{d\bar{r}} = \frac{\psi}{2\bar{r}} \left(\sqrt{1 - \frac{2m}{r}} - 1 \right), \quad (\text{B10})$$

$$\frac{d\alpha}{d\bar{r}} = \alpha \frac{m + 4\pi r^3 p}{\sqrt{1 - 2m/r}} \frac{1}{r\bar{r}}, \quad (\text{B11})$$

where we used Eq. (B6) to derive Eqs. (B10) and (B11). It is possible to simply integrate the system above to obtain the star profile in isotropic coordinates. Initial values at $\bar{r} = 0$ are needed, and although this is not a problem for r , m , and p (the latter being in general a free parameter), but the values of α , ψ are not available to have a smooth matching at the surface of the star $\bar{r} = \bar{R}$, whose position is still unknown. On the other hand, one way to obtain a smooth solution across the star’s surface is to exploit the coordinate transformations

$$r = \bar{r} \left(1 + \frac{M}{2\bar{r}} \right)^2, \quad (\text{B12})$$

$$\bar{r} = \frac{r}{2} \left[1 + \sqrt{1 - \frac{2M}{r}} - \frac{M}{r} \right], \quad (\text{B13})$$

to derive the expressions of ψ , α in the Schwarzschild coordinates

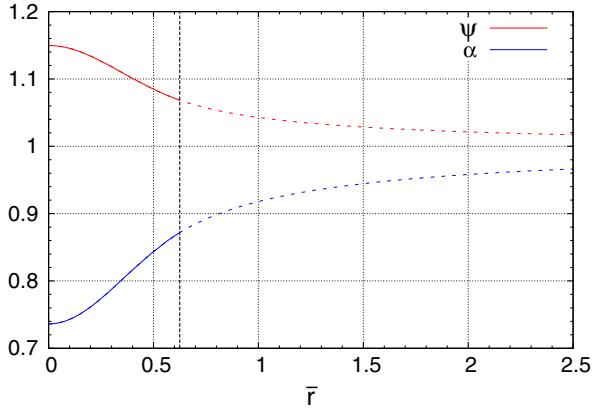


FIG. 12 (color online). Solution of isotropic TOV using correct boundary conditions. A rescaling was done at the surface to be at $\bar{r} = 0.625$.

$$\psi(r) = \frac{r}{M} \left(1 - \sqrt{1 - \frac{2M}{r}} \right), \quad (\text{B14})$$

$$\alpha(r) = \sqrt{1 - \frac{2M}{r}}. \quad (\text{B15})$$

Again making use of Eq. (B7) and of the analytic integration of its left-hand side, Eq. (B10) can be written as

$$d \ln \psi = F(r, m(r)) dr, \quad (\text{B16})$$

where

$$F(r, m(r)) := \frac{1}{2r} \left(1 - \frac{1}{\sqrt{1 - 2m(r)/r}} \right). \quad (\text{B17})$$

As a result, an integration between $r = 0$ and $r = R$ of $F(r, m)$ leads to the following condition for the conformal factor ψ :

$$\psi(0) = \psi(R) \exp \left[- \int_0^R F(r, m(r)) dr \right], \quad (\text{B18})$$

so that ψ (and similarly α) at the star's surface are guaranteed to match smoothly the exterior solution, as it can be seen in Fig. 12.

APPENDIX C: ITERATION SCHEME

The iteration procedure for binary stars is similar to the one for binary black holes described in Ref. [73], but it also contains the fluid coordinates and a solution for the extra fluid variables in a multipatch setting. An overall picture of this procedure is shown in Fig. 13, where the steps of the gravitational Poisson solver (essentially everything from “Compute S_ψ ” up to “Invert ∇^2 , compute ψ ”) have been described in detail in [73].

The code first initializes the lapse function and the conformal factor from some initial spherical solution. For that purpose we have developed two methods. One is an isotropic TOV solver (see Appendix B), and another is a one-dimensional KEH method. This last choice reproduces the KEH approach used in three-dimensional computations, but in a one-dimensional mesh. Included in this method are all the important ingredients of the three-dimensional code, such as the renormalization of variables. Comparing the results from these two independent schemes gives us confidence about the robustness of the COCAL iterative solutions.

After a choice of the velocity fluid potential, of the orbital angular velocity, and in the case of spinning binaries, also of the rotational states of each compact object, the code proceeds to the main part of the iteration, which always starts by interpolating $q = p/\rho$, $\partial_i \Phi$, and \tilde{s}^i from the surface-fitted coordinates to the gravitational coordinates. The interpolated quantities are then used in the gravitational Poisson solver, which is executed in addition to the root-finding routine explained in Sec. III B. As discussed there, the constants related to the Euler integral, the orbital angular velocity, and the scaling of our grids C , $\hat{\Omega}$, R_0 , are calculated at this point, and the lapse function, as well as the conformal factor, are updated according to

$$\psi^{\text{new}} = (\psi^{\text{old}})^{(R_0^{\text{new}}/R_0^{\text{old}})^2}, \quad \alpha^{\text{new}} = (\alpha^{\text{old}})^{(R_0^{\text{new}}/R_0^{\text{old}})^2}. \quad (\text{C1})$$

When the gravitational solver ends, ψ , β^i , α are interpolated to the surface-fitted coordinates in preparation for the fluid Poisson solver. The main steps now are the computation of the new value of q , by the use of Eq. (49) or Eq. (32), and then the solution of the conservation of rest mass, Eq. (57). At this point, also the surface of the star is computed.

At each iteration step, the fluid computation is performed a few times (4 times for the results presented here) since this results in a more stable final computation. A relaxation parameter ξ is used when updating a newly computed variable. If $\Phi^{(n)}(x)$ is the n th step value, and $\hat{\Phi}(x)$ the result of the Poisson solver, then the $(n+1)$ th step value will be

$$\Phi^{(n+1)}(x) := \xi \hat{\Phi}(x) + (1 - \xi) \Phi^{(n)}(x), \quad (\text{C2})$$

where $0.1 \leq \xi \leq 0.4$. Usually $\xi = 0.4$ for α , ψ , β^i , q , while $\xi = 0.1$ for ϕ .

The criterion used by COCAL to stop the iteration is given by

$$2 \frac{|\Phi^{(n)} - \Phi^{(n-1)}|}{|\Phi^{(n)}| + |\Phi^{(n-1)}|} < \epsilon_c, \quad (\text{C3})$$

for all points of the grids, and all variables α , ψ , β^i , q , Φ , where we used $\epsilon_c = 10^{-6}$ in this paper. In almost all of our calculations, ψ and α converge to machine precision,

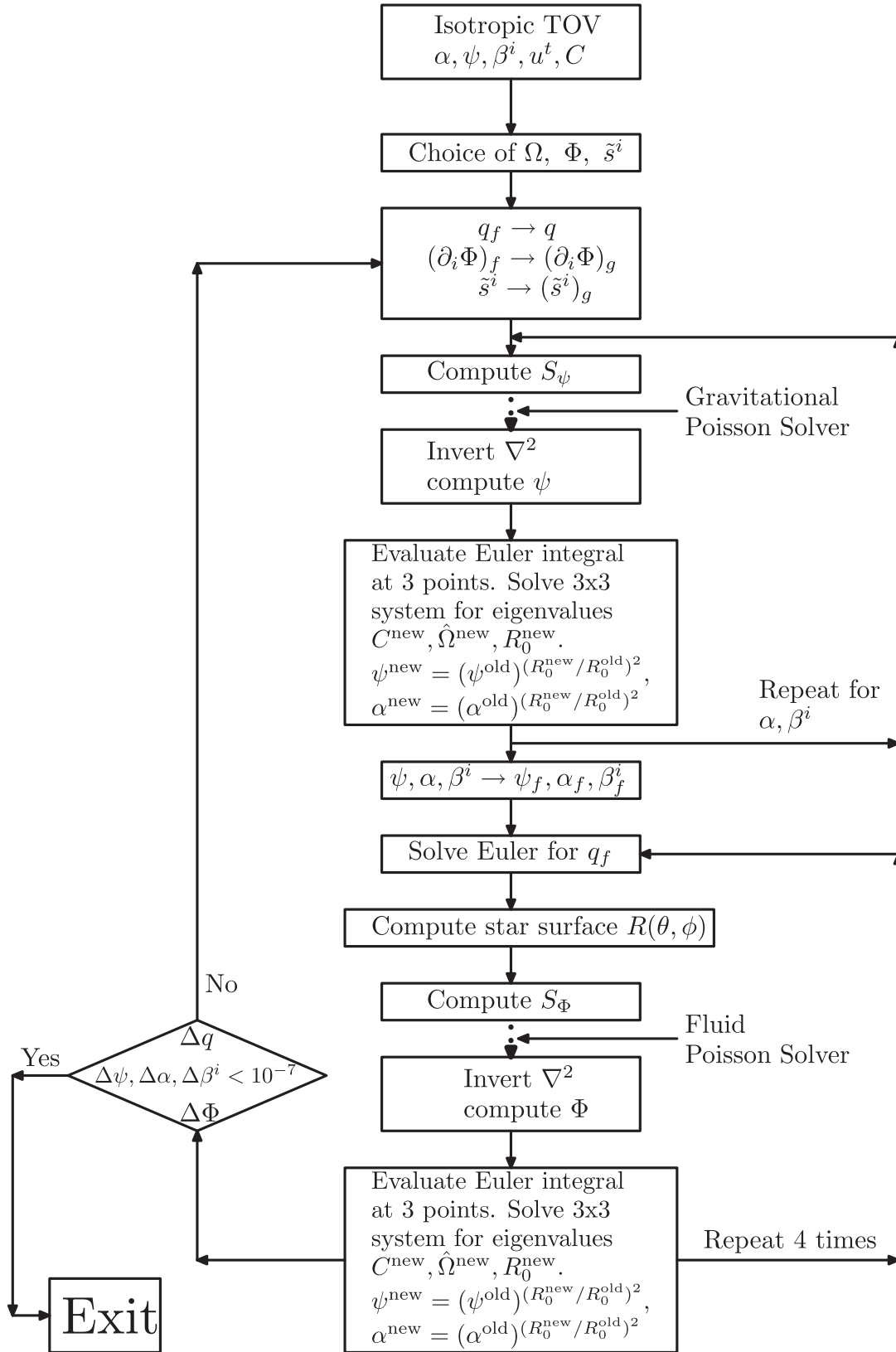


FIG. 13. The COCAL iteration for spinning binary stars.

TABLE V. Grid parameters used for the irrotational and spinning sequences with the APR1 EOS, presented in Fig. 10.

Type	Patch	r_a	r_s	r_b	r_c	r_e	N_r^f	N_r^l	N_r^m	N_r	N_θ	N_ϕ	L
Hs2.5d	COCP-1	0.0	var	10^2	1.25	1.125	76	96	120	288	72	72	12
	COCP-2	0.0	var	10^2	1.25	1.125	76	96	120	288	72	72	12
	ARCP	5.0	...	10^6	6.25	...	24	...	30	192	72	72	12

TABLE VI. Grid parameters used for the white-dwarf solutions with $\Gamma = 5/3$.

Type	Patch	r_a	r_s	r_b	r_c	r_e	N_r^f	N_r^l	N_r^m	N_r	N_θ	N_ϕ	L
WD	COCP-1	0.0	1.0	10^2	1.50	1.25	64	64	96	192	144	144	12
	COCP-2	0.0	1.0	10^2	1.50	1.25	64	64	96	192	144	144	12
	ARCP	5.0	...	10^6	6.25	...	16	...	20	192	144	144	12

while the error in the fluid variables q and Φ decreases to $\approx 10^{-12}$ before the error in the shift reaches 10^{-7} . This is due to the existence of points in the gravitational mesh where the shift has almost zero values, and convergence is much slower there. Neglecting such points can speed up a solution by a factor of at least 2. Currently, COCAL is running on a serial processor, and it needs around 3–4 GB of RAM to produce the solutions presented in this work. With an Intel Xeon 3.60 GHz processor, about two days are needed for these computations, with the irrotational configurations taking longer than the spinning ones; this is not a surprise since convergence is faster for corotating binaries.

APPENDIX D: COROTATING BINARY WHITE DWARFS

To test the sensitivity of our code and to prepare for future work concerning neutron star-white dwarf or black hole-white dwarf binaries, we also compute a corotating binary white dwarf solution. Here the fields are orders of

magnitude less than the ones encountered in typical binary neutron star binaries, and greater resolution is required in order to acquire smooth solutions. The resolution used is reported in Table VI where we can see that an increase in N_θ, N_ϕ by a factor of 3 relative to the solutions obtained in Fig. 2, Table II, was used. In Fig. 14 we show a representative binary white dwarfs solution with compactness $\mathcal{C} = 2 \times 10^{-4}$, with centers placed at $x = \pm 1.25$ and unit radii. From left to right, the different panels report the contour plot of the lapse function from 0.9994 to 1.0 with a step of 2×10^{-5} , the shift vector field, and the contour plot of the rest mass density. Note that the plots are centered at the origin of the COCP-1 patch and the green circle refers to the excised sphere S_e . Values inside S_e are taken from the COCP-2 patch. The shift vector in binary white dwarfs is approximately 4 orders of magnitude smaller than the one typically encountered in neutron stars, while the quantity $|\alpha - 1|$ is about 3 orders of magnitude smaller. Overall we see a good convergence between the different coordinate systems even for these small values of the metric quantities.

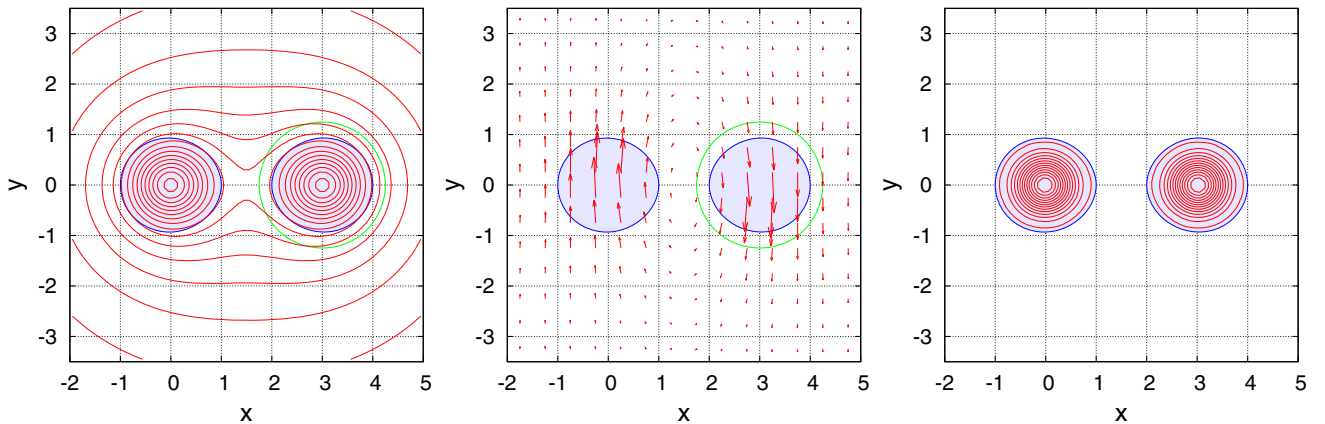


FIG. 14 (color online). Binary white dwarfs solution with compactness $\mathcal{C} = 2 \times 10^{-4}$, stellar centers placed at $x = \pm 1.25$ and unit radii. Shown from left to right are a contour plot of the lapse function from 0.9994 to 1.0 with step of 2×10^{-5} , the shift vector field with maximum value 8.4×10^{-6} , and a contour plot of the rest-mass density from 2×10^{-8} to 10^{-4} with step 8×10^{-8} . Note that the green sphere corresponds to the excised sphere S_e of COCP-1.

APPENDIX E: POST-NEWTONIAN APPROXIMATION

The 4PN approximation for the binding energy of a system of two nonspinning bodies with masses M_1, M_2 and in quasicircular orbit has been used in Fig. 10 to compare with the numerical results of irrotational and spinning binaries. The explicit expression is given by [125–127]

$$\begin{aligned} \frac{E_{\text{irr}}}{Mc^2} = & -\frac{\nu x}{2} \left\{ 1 + \left(-\frac{3}{4} - \frac{1}{12}\nu \right) x + \left(-\frac{27}{8} + \frac{19}{8}\nu - \frac{1}{24}\nu^2 \right) x^2 + \left[-\frac{675}{64} + \left(\frac{34445}{576} - \frac{205}{96}\pi^2 \right) \nu - \frac{155}{96}\nu^2 - \frac{35}{5184}\nu^3 \right] x^3 \right. \\ & + \left[-\frac{3969}{128} + \left(-\frac{123671}{5760} + \frac{9037}{1536}\pi^2 + \frac{1792}{15}\ln 2 + \frac{896}{15}\gamma_E \right) \nu \right. \\ & \left. \left. + \left(-\frac{498449}{3456} + \frac{3157}{576}\pi^2 \right) \nu^2 + \frac{301}{1728}\nu^3 + \frac{77}{31104}\nu^4 + \frac{448}{15}\nu \ln x \right] x^4 \right\}, \end{aligned} \quad (\text{E1})$$

where γ_E is the Euler constant, $M := M_1 + M_2$ is the total mass of the system, $\nu := M_1 M_2 / M^2$ is the symmetric mass ratio, and x is the dimensionless orbital frequency

$$x := \left(\frac{\Omega GM}{c^3} \right)^{2/3}. \quad (\text{E2})$$

For a corotating binary the binding energy also includes terms from the kinetic energy of the spins as well as from the spin orbit interaction. To 3PN this extra contribution is

$$\frac{\Delta E_{\text{cor}}}{Mc^2} = (2 - 6\nu)x^3 + (-10\nu + 25\nu^2)x^4, \quad (\text{E3})$$

and therefore the total binding energy is given by the sum of (E1) and (E3).

For a system that satisfies the first law of binary mechanics and has binding energy of the form

$$E_b(x) = \sum_{i=1}^N (A_i + B_i \ln x) x^{i/2} \quad (\text{E4})$$

the angular momentum will be

$$J(x) = \sum_{i=1}^N \left[\frac{i}{i-3} (A_i + B_i \ln x) - \frac{6B_i}{(i-3)^2} \right] x^{\frac{i-3}{2}}. \quad (\text{E5})$$

Using (E5) the irrotational part of the angular momentum is

$$\begin{aligned} \frac{J_{\text{irr}}}{GM^2/c} = & \frac{\nu}{\sqrt{x}} \left\{ 1 + \left(\frac{3}{2} + \frac{1}{6}\nu \right) x + \left(\frac{27}{8} - \frac{19}{8}\nu + \frac{1}{24}\nu^2 \right) x^2 + \left[\frac{135}{16} + \left(-\frac{6889}{144} + \frac{41}{24}\pi^2 \right) \nu + \frac{31}{24}\nu^2 + \frac{7}{1296}\nu^3 \right] x^3 \right. \\ & + \left[\frac{2835}{128} + \left(\frac{98869}{5760} - \frac{6455}{1536}\pi^2 - \frac{256}{3}\ln 2 - \frac{128}{3}\gamma_E \right) \nu \right. \\ & \left. \left. + \left(\frac{356035}{3456} - \frac{2255}{576}\pi^2 \right) \nu^2 - \frac{215}{1728}\nu^3 - \frac{55}{31104}\nu^4 - \frac{64}{3}\nu \ln x \right] x^4 \right\}, \end{aligned} \quad (\text{E6})$$

while the corotating additional part is

$$\frac{\Delta J_{\text{cor}}}{GM^2/c} = (4 - 12\nu)x^{3/2} + (-16\nu + 40\nu^2)x^{5/2}. \quad (\text{E7})$$

- [1] M. Shibata and K. Uryū, *Phys. Rev. D* **61**, 064001 (2000).
 [2] L. Baiotti, B. Giacomazzo, and L. Rezzolla, *Phys. Rev. D* **78**, 084033 (2008).
 [3] M. Anderson, E. W. Hirschmann, L. Lehner, S. L. Liebling, P. M. Motl, D. Neilsen, C. Palenzuela, and J. E. Tohline, *Phys. Rev. D* **77**, 024006 (2008).

- [4] Y. T. Liu, S. L. Shapiro, Z. B. Etienne, and K. Taniguchi, *Phys. Rev. D* **78**, 024012 (2008).
 [5] S. Bernuzzi, M. Thierfelder, and B. Brügmann, *Phys. Rev. D* **85**, 104030 (2012).
 [6] R. Narayan, B. Paczynski, and T. Piran, *Astrophys. J.* **395**, L83 (1992).

- [7] D. Eichler, M. Livio, T. Piran, and D. N. Schramm, *Nature (London)* **340**, 126 (1989).
- [8] E. Berger, *Annu. Rev. Astron. Astrophys.* **52**, 43 (2014).
- [9] L. Rezzolla, B. Giacomazzo, L. Baiotti, J. Granot, C. Kouveliotou, and M. A. Aloy, *Astrophys. J.* **732**, L6 (2011).
- [10] V. Paschalidis, M. Ruiz, and S. L. Shapiro, arXiv:1410.7392.
- [11] J. M. Lattimer and D. N. Schramm, *Astrophys. J.* **192**, L145 (1974).
- [12] L.-X. Li and B. Paczynski, *Astrophys. J.* **507**, L59 (1998).
- [13] N. R. Tanvir, A. J. Levan, A. S. Fruchter, J. Hjorth, R. A. Hounsell, K. Wiersema, and R. L. Tunnicliffe, *Nature (London)* **500**, 547 (2013).
- [14] E. Berger, W. Fong, and R. Chornock, *Astrophys. J.* **774**, L23 (2013).
- [15] M. Tanaka and K. Hotokezaka, *Astrophys. J.* **775**, 113 (2013).
- [16] S. Rosswog, O. Korobkin, A. Arcones, F.-K. Thielemann, and T. Piran, *Mon. Not. R. Astron. Soc.* **439**, 744 (2014).
- [17] F. A. Rasio and S. L. Shapiro, *Classical Quantum Gravity* **16**, R1 (1999).
- [18] N. Andersson, V. Ferrari, D. I. Jones, K. D. Kokkotas, B. Krishnan, J. S. Read, L. Rezzolla, and B. Zink, *Gen. Relativ. Gravit.* **43**, 409 (2011).
- [19] A. Abramovici *et al.*, *Science* **256**, 325 (1992).
- [20] T. Accadia *et al.*, *Classical Quantum Gravity* **28**, 025005 (2011).
- [21] K. Kuroda, *Classical Quantum Gravity* **27**, 084004 (2010).
- [22] Y. Aso, Y. Michimura, K. Somiya, M. Ando, O. Miyakawa, T. Sekiguchi, D. Tatsumi, and H. Yamamoto, *Phys. Rev. D* **88**, 043007 (2013).
- [23] M. Punturo *et al.*, *Classical Quantum Gravity* **27**, 084007 (2010).
- [24] J. Abadie *et al.*, *Classical Quantum Gravity* **27**, 173001 (2010).
- [25] E. E. Flanagan and T. Hinderer, *Phys. Rev. D* **77**, 021502 (R) (2008).
- [26] T. Hinderer, *Astrophys. J.* **677**, 1216 (2008).
- [27] T. Hinderer, B. D. Lackey, R. N. Lang, and J. S. Read, *Phys. Rev. D* **81**, 123016 (2010).
- [28] T. Damour, A. Nagar, and L. Villain, *Phys. Rev. D* **85**, 123007 (2012).
- [29] K. Takami, L. Rezzolla, and L. Baiotti, *Phys. Rev. Lett.* **113**, 091104 (2014).
- [30] A. Bauswein and H.-T. Janka, *Phys. Rev. Lett.* **108**, 011101 (2012).
- [31] J. S. Read, L. Baiotti, J. D. E. Creighton, J. L. Friedman, B. Giacomazzo, K. Kyutoku, C. Markakis, L. Rezzolla, M. Shibata, and K. Taniguchi, *Phys. Rev. D* **88**, 044042 (2013).
- [32] S. Bernuzzi, A. Nagar, S. Balmelli, T. Dietrich, and M. Ujevic, *Phys. Rev. Lett.* **112**, 201101 (2014).
- [33] K. Takami, L. Rezzolla, and L. Baiotti, *Phys. Rev. D* **91**, 064001 (2015).
- [34] C. S. Kochanek, *Astrophys. J.* **398**, 234 (1992).
- [35] L. Bildsten and C. Cutler, *Astrophys. J.* **400**, 175 (1992).
- [36] L. Rezzolla and O. Zanotti, *Relativistic Hydrodynamics* (Oxford University Press, Oxford, UK, 2013).
- [37] J. Isenberg, *Int. J. Mod. Phys. D* **17**, 265 (2008); J. Isenberg and J. Nester, in *General Relativity and Gravitation*, edited by A. Held (Plenum, New York, 1980), Vol. 1.
- [38] J. R. Wilson and G. J. Mathews, in *Frontiers in Numerical Relativity*, edited by C. R. Evans, L. S. Finn, and D. W. Hobill (Cambridge University Press, Cambridge, UK, 1989).
- [39] S. Bonazzola, E. Gourgoulhon, and J.-A. Marck, *Phys. Rev. D* **56**, 7740 (1997).
- [40] M. Shibata, *Phys. Rev. D* **58**, 024012 (1998).
- [41] S. A. Teukolsky, *Astrophys. J.* **504**, 442 (1998).
- [42] H. Asada, *Phys. Rev. D* **57**, 7292 (1998).
- [43] K. Taniguchi and E. Gourgoulhon, *Phys. Rev. D* **66**, 104019 (2002).
- [44] S. Bonazzola, E. Gourgoulhon, and J.-A. Marck, *Phys. Rev. Lett.* **82**, 892 (1999).
- [45] P. Marronetti, G. J. Mathews, and J. R. Wilson, *Phys. Rev. D* **60**, 087301 (1999).
- [46] K. Uryū and Y. Eriguchi, *Phys. Rev. D* **61**, 124023 (2000).
- [47] K. Uryū, M. Shibata, and Y. Eriguchi, *Phys. Rev. D* **62**, 104015 (2000).
- [48] E. Gourgoulhon, P. Grandclément, K. Taniguchi, J.-A. Marck, and S. Bonazzola, *Phys. Rev. D* **63**, 064029 (2001).
- [49] K. Taniguchi and E. Gourgoulhon, *Phys. Rev. D* **68**, 124025 (2003).
- [50] F. Limousin, D. Gondek-Rosinska, and E. Gourgoulhon, *Phys. Rev. D* **71**, 064012 (2005).
- [51] M. Bejger, D. Gondek-Rosinska, E. Gourgoulhon, P. Haensel, K. Taniguchi, and J. L. Zdenik, *Astron. Astrophys.* **431**, 297 (2005).
- [52] W. Tichy, *Classical Quantum Gravity* **26**, 175018 (2009).
- [53] K. Taniguchi and M. Shibata, *Astrophys. J. Suppl. Ser.* **188**, 187 (2010).
- [54] M. Shibata, K. Uryū, and J. L. Friedman, *Phys. Rev. D* **70**, 044044 (2004).
- [55] K. Uryū, F. Limousin, J. L. Friedman, E. Gourgoulhon, and M. Shibata, *Phys. Rev. Lett.* **97**, 171101 (2006).
- [56] K. Uryū, F. Limousin, J. L. Friedman, E. Gourgoulhon, and M. Shibata, *Phys. Rev. D* **80**, 124004 (2009).
- [57] G. Schäfer and A. Gopakumar, *Phys. Rev. D* **69**, 021501 (R) (2004).
- [58] S. Bonazzola, E. Gourgoulhon, P. Grandclément, and J. Novak, *Phys. Rev. D* **70**, 104007 (2004).
- [59] S. Yoshida, B. C. Bromley, J. S. Read, K. Uryū, and J. L. Friedman, *Classical Quantum Gravity* **23**, S599 (2006).
- [60] H. P. Pfeiffer, D. A. Brown, L. E. Kidder, L. Lindblom, G. Lovelace, and M. A. Scheel, *Classical Quantum Gravity* **24**, S59 (2007).
- [61] K. Kyutoku, M. Shibata, and K. Taniguchi, *Phys. Rev. D* **90**, 064006 (2014).
- [62] N. Moldenhauer, C. M. Markakis, N. K. Johnson-McDaniel, W. Tichy, and B. Bruegmann, *Phys. Rev. D* **90**, 084043 (2014).
- [63] W. Tichy, *Phys. Rev. D* **84**, 024041 (2011).
- [64] D. R. Lorimer, *Living Rev. Relativity* **11**, 8 (2008).
- [65] P. Marronetti and S. L. Shapiro, *Phys. Rev. D* **68**, 104024 (2003).
- [66] T. W. Baumgarte and S. L. Shapiro, *Phys. Rev. D* **80**, 064009 (2009).
- [67] W. Tichy, *Phys. Rev. D* **86**, 064024 (2012).
- [68] P. Tsatsin and P. Marronetti, *Phys. Rev. D* **88**, 064060 (2013).

- [69] W. Kastaun, F. Galeazzi, D. Alic, L. Rezzolla, and J. A. Font, *Phys. Rev. D* **88**, 021501(R) (2013).
- [70] S. Bernuzzi, T. Dietrich, W. Tichy, and B. Bruggmann, *Phys. Rev. D* **89**, 104021 (2014).
- [71] X. Huang, C. Markakis, N. Sugiyama, and K. Uryū, *Phys. Rev. D* **78**, 124023 (2008).
- [72] K. Uryū, E.ourgoulhon, C. M. Markakis, K. Fujisawa, A. Tsokaros, and Y. Eriguchi, *Phys. Rev. D* **90**, 101501(R) (2014).
- [73] K. Uryū and A. Tsokaros, *Phys. Rev. D* **85**, 064014 (2012).
- [74] K. Uryū, A. Tsokaros, and P. Grandclément, *Phys. Rev. D* **86**, 104001 (2012).
- [75] A. Tsokaros and K. Uryū, *J. Eng. Math.* **82**, 133 (2013).
- [76] J. P. Ostriker and J. W.-K. Mark, *Astrophys. J.* **151**, 1075 (1968).
- [77] I. Hachisu, *Astrophys. J. Suppl. Ser.* **61**, 479 (1986).
- [78] I. Hachisu, *Astrophys. J. Suppl. Ser.* **62**, 461 (1986).
- [79] I. Hachisu, Y. Eriguchi, and K. Nomaoto, *Astrophys. J.* **308**, 161 (1986).
- [80] I. Hachisu, Y. Eriguchi, and K. Nomaoto, *Astrophys. J.* **311**, 214 (1986).
- [81] H. Komatsu, Y. Eriguchi, and I. Hachisu, *Mon. Not. R. Astron. Soc.* **237**, 355 (1989).
- [82] A. Tsokaros and K. Uryū, *Phys. Rev. D* **75**, 044026 (2007).
- [83] K. Uryū and Y. Eriguchi, *Astrophys. J. Suppl.* **118**, 563 (1998).
- [84] C. W. Misner, K. S. Thorne, and J. A. Wheeler, *Gravitation* (Freeman, San Francisco, 1973).
- [85] J. W. York, in *Sources of Gravitational Radiation*, edited by L. Smarr (Cambridge University Press, Cambridge, UK, 1979).
- [86] G. B. Cook, *Living Rev. Relativity* **3**, 5 (2000).
- [87] E.ourgoulhon, *3+1 Formalism in General Relativity: Bases of Numerical Relativity*, Lecture Notes in Physics Vol. 846 (Springer, New York, 2012).
- [88] J. K. Blackburn and S. Detweiler, *Phys. Rev. D* **46**, 2318 (1992).
- [89] S. Detweiler, *Phys. Rev. D* **50**, 4929 (1994).
- [90] A. Schild, *Phys. Rev.* **131**, 2762 (1963).
- [91] J. L. Friedman and K. Uryū, *Phys. Rev. D* **73**, 104039 (2006).
- [92] M. M. Glenz and K. Uryū, *Phys. Rev. D* **76**, 027501 (2007).
- [93] J. L. Friedman, K. Uryū, and M. Shibata, *Phys. Rev. D* **65**, 064035 (2002).
- [94] E.ourgoulhon, P. Grandclément, and S. Bonazzola, *Phys. Rev. D* **65**, 044020 (2002).
- [95] P. Grandclément, E.ourgoulhon, and S. Bonazzola, *Phys. Rev. D* **65**, 044021 (2002).
- [96] M. Alcubierre, *Introduction to 3+1 Numerical Relativity* (Oxford University Press, New York, 2008).
- [97] T. W. Baumgarte and S. L. Shapiro, *Numerical Relativity: Solving Einstein's Equations on the Computer* (Cambridge University Press, Cambridge, UK, 2010).
- [98] J. L. Friedman and N. Stergioulas, *Rotating Relativistic Stars*, Cambridge Monographs on Mathematical Physics (Cambridge University Press, Cambridge, UK, 2013).
- [99] R. H. Boyer, *Proc. Cambridge Philos. Soc.* **61**, 527 (1965).
- [100] J. M. Bardeen and R. V. Wagoner, *Astrophys. J.* **167**, 359 (1971).
- [101] J. S. Read, B. D. Lackey, B. J. Owen, and J. L. Friedman, *Phys. Rev. D* **79**, 124032 (2009).
- [102] J. S. Read, C. Markakis, M. Shibata, K. Uryū, J. D. E. Creighton, and J. L. Friedman, *Phys. Rev. D* **79**, 124033 (2009).
- [103] F. Douchin and P. Haensel, *Astron. Astrophys.* **380**, 151 (2001).
- [104] A. Akmal, V. R. Pandharipande, and D. G. Ravenhall, *Phys. Rev. C* **58**, 1804 (1998).
- [105] K. Uryū and Y. Eriguchi, *Mon. Not. R. Astron. Soc.* **299**, 575 (1998).
- [106] T. W. Baumgarte, G. B. Cook, M. A. Scheel, S. L. Shapiro, and S. A. Teukolsky, *Phys. Rev. D* **57**, 7299 (1998).
- [107] A. Komar, *Phys. Rev.* **113**, 934 (1959).
- [108] A. Komar, *Phys. Rev.* **127**, 1411 (1962).
- [109] R. Beig, *Phys. Lett.* **69A**, 153 (1978).
- [110] A. Ashtekar and A. Magnon-Ashtekar, *J. Math. Phys. (N.Y.)* **20**, 793 (1979).
- [111] E.ourgoulhon and S. Bonazzola, *Classical Quantum Gravity* **11**, 443 (1994).
- [112] P. Marronetti, G. J. Mathews, and J. R. Wilson, *Phys. Rev. D* **58**, 107503 (1998).
- [113] F. Usui, K. Uryū, and Y. Eriguchi, *Phys. Rev. D* **61**, 024039 (1999).
- [114] F. Usui and Y. Eriguchi, *Phys. Rev. D* **65**, 064030 (2002).
- [115] LORENE Web site, <http://www.lorene.obspm.fr/>.
- [116] J. R. Wilson, G. J. Mathews, and P. Marronetti, *Phys. Rev. D* **54**, 1317 (1996).
- [117] T. W. Baumgarte, G. B. Cook, M. A. Scheel, S. L. Shapiro, and S. A. Teukolsky, *Phys. Rev. D* **57**, 6181 (1998).
- [118] E. E. Flanagan, *Phys. Rev. Lett.* **82**, 1354 (1999).
- [119] G. J. Mathews and J. R. Wilson, *Phys. Rev. D* **61**, 127304 (2000).
- [120] L. E. Kidder, C. W. Will, and A. G. Wiseman, *Phys. Rev. D* **47**, R4183 (1993).
- [121] L. E. Kidder, *Phys. Rev. D* **52**, 821 (1995).
- [122] M. Campanelli, C. O. Lousto, and Y. Zlochower, *Phys. Rev. D* **74**, 041501(R) (2006).
- [123] L. Rezzolla, P. Diener, E. N. Dorband, D. Pollney, C. Reisswig, E. Schnetter, and J. Seiler, *Astrophys. J. Lett.* **674**, L29 (2008).
- [124] E. Barausse and L. Rezzolla, *Astrophys. J. Lett.* **704**, L40 (2009).
- [125] D. Bini and T. Damour, *Phys. Rev. D* **87**, 121501 (2013).
- [126] T. Damour, P. Jaranowski, and G. Schäfer, *Phys. Rev. D* **89**, 064058 (2014).
- [127] L. Blanchet, *Living Rev. Relativity* **17**, 2 (2014).
- [128] A. Bohé, S. Marsat, G. Faye, and L. Blanchet, *Classical Quantum Gravity* **30**, 075017 (2013).
- [129] D. Radice, L. Rezzolla, and F. Galeazzi, *Mon. Not. R. Astron. Soc. Lett.* **437**, L46 (2014).
- [130] D. Radice, L. Rezzolla, and F. Galeazzi, *Classical Quantum Gravity* **31**, 075012 (2014).